CHEMISTRY OF MATERIALS

pubs.acs.org/cm

Article

Structural Analysis and Redox Properties of Oxygen-"Breathing" $A(Mn_{1-x}Cu_x)O_3$ (A = La, Pr) Perovskites

Gregor Koch, Giulia Bellini, Frank Girgsdies, Michael Hävecker, Spencer J. Carey, Olaf Timpe, Thomas Götsch, Thomas Lunkenbein, Gudrun Auffermann, Andrey Tarasov, Robert Schlögl, and Annette Trunschke*

Cite This: https://doi.org/10.1021/acs.chemmater.4c00136

Read Online

ACCESS | Metrics & More | Article Recommendations | Supporting Information

ABSTRACT: The redox properties of perovskites play an important role in their use in thermo- and electrocatalytic applications. Here, we report the effects of substituting copper for manganese in $A(Mn_{1-x}Cu_x)O_3$ (A = La, Pr; $0 \leq x \leq 0.4$) perovskites on structural and chemical properties when lanthanum and praseodymium are used as A cations, whereas the synthesis of Pr-based materials has not been reported so far. On the one hand, we investigate the influence of the Cu content on the crystal structure and the surface composition of the materials and, on the other hand, how the composition affects the redox properties of the materials under reduction with H_2 and reoxidation. The detailed refinement of X-ray diffraction data revealed that complex structural changes occur with increasing substitution, which, however, do not correlate linearly with the copper content and proceed differently for the La- and Pr-based systems with octahedral tilting as the main degree of freedom. While the structure of La-based perovskites changes with Cu content from the rhombohedral $LaAlO_3$ structural type ($x < 0.2$) to the orthorhombic $GdFeO_3$ type ($x > 0.2$), $Pr(Mn_{1-x}Cu_x)O_3$ perovskites form an O′-orthorhombic $GdFeO_3$-type structure over the whole composition range. In the temperature range up to 300 °C, which is important for low-temperature catalysis, the perovskites studied are structurally stable in redox reactions with hydrogen and oxygen in the sense that segregation of secondary phases essentially does not occur. However, the perovskites take up and release oxygen reversibly, which is reflected in the reversible changes of the normalized unit cell volume and can be pictorially compared to the breathing in and out of lattice oxygen, the capacity of which clearly correlates with the copper content. Nevertheless, the readily available lattice oxygen neither leads to higher activity in propane oxidation, which is used as a probe reaction, nor does it have a negative effect on the selectivity of the valuable product propene, which is in clear contrast to common concepts in oxidation catalysis. In addition, there is no simple correlation between the structural parameters of the bulk and properties in catalysis. The perovskites thus serve as a carrier and reservoir for a catalytically active Mn-oxide surface phase in low-temperature redox catalysis.

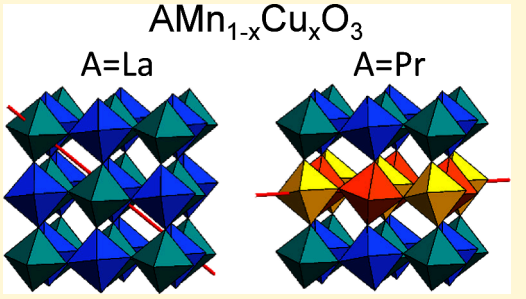

INTRODUCTION

The chemical variability and stability of perovskites, which can be described by the general formula ABO_3, enable multiple applications of these mixed oxides in catalysis,[1] photoelectrochemistry,[2,3] superconductivity,[4,5] magneto-resistive effects,[6,7] or ion diffusion.[8] Since the 1970s, strategies have been implemented to optimize the properties of perovskites for their use in catalysis, especially in redox catalysis, in which the defect structure is adopted by adjusting the valence of A and B.[9]

Manganite perovskites alone open up an enormous variability, as manganese can occur on the B-site as Mn^{2+}, Mn^{3+}, and Mn^{4+}. In addition, the average oxidation state of manganese can be tuned by choosing a specific A-site element, e.g., lanthanides, or by choosing a combination of A-site elements, e.g., lanthanides and alkaline earth elements. The oxidation state of manganese can also be influenced by the partial substitution of manganese with another B element if the A element is kept constant. If the formal oxidation state of one of the metals in the perovskite structure differs from 3+, the charge can be balanced by creating vacancies in the lattice where A-site deficiency, B-site deficiency, or oxygen deficiency can occur.[10−12] This diversity in defect structure is reflected in the wide phase space of manganites.[13,14]

The cooperation of two different B-site elements in the stabilization of unusual oxidation states has previously been identified as an effective tool for optimizing the functionality of perovskites with respect to the activation of reacting molecules at the gas−solid interface in catalysis.[15−26] Multicomponent

Received: January 16, 2024
Revised: April 30, 2024
Accepted: May 1, 2024

materials were synthesized either by the Pechini method,[19] the citrate method,[22] or by freeze-drying of sols obtained from metal acetates.[17,18,20,24,25] The substitution of manganese by copper in $La(Mn_{1-x}Cu_x)O_3$ perovskites has been studied repeatedly in oxidation reactions, in particular for CO oxidation.[16−23] A synergistic effect of Cu and Mn was postulated, which was attributed to the fact that Mn and Cu share the functions in CO oxidation, with Mn−O being responsible for the activation of oxygen and the Cu ions for the adsorption of carbon monoxide.[18] It has also been suggested that substitution increases the oxygen mobility within the perovskite lattice and thus the activity in oxidation reactions.[23] In a study that mainly focused on the synthesis of $La(Mn_{1-x}Cu_x)O_3$ perovskites, it was shown that nonstoichiometry (excess or defect oxygen) can be adjusted by the copper content.[24] The redox properties of $La(Mn_{1-x}Cu_x)O_3$ and the Mn^{3+}/Mn^{4+} ratios were determined by temperature-programmed reduction.[19,20,23,24] However, there is still the open question of whether the inserted Cu^{2+} destabilizes the perovskite structure under reducing conditions or whether the inserted Cu^{2+} tunes the amount of oxygen that can be released as it has been reported for A-site substitution of A^{3+} by A'^{2+}, e.g., by an alkaline earth element.[26] In particular, the influence of the amount of oxygen that can be reversibly removed and incorporated into selective oxidation reactions over perovskites has not yet been studied in detail.

Therefore, in the present work, two series of $A(Mn_{1-x}Cu_x)O_3$ perovskites ($0 \le x \le 0.4$; A = La, Pr) were synthesized by solution combustion synthesis.[27] It is observed that both the Cu content,[18] and the calcination conditions (temperature and gas composition) influence whether the Cu-containing lanthanum manganites adopt rhombohedral or orthorhombic symmetry.[28] Changes in the structure are related to the tilting or buckling of the corner-sharing BO_6 octahedra, which is different from the straight-line arrangement of the BO_6 octahedra in the ideal cubic perovskite structure. Using Pr^{3+} for population of the A-sites, which is smaller compared to La^{3+}, a new series of $Pr(Mn_{1-x}Cu_x)O_3$ ($0 \le x \le 0.4$) perovskites can be reported here for the first time, forming exclusively an orthorhombic $GdFeO_3$ type structure over the entire compositional range studied. Making this series available allows us to investigate the change in redox properties due to Cu substitution without having to consider structural transformations at the same time. Our analysis of surface composition and structural changes during redox reactions provide important insights for the use of $A(B,B')O_3$ perovskites in applications where the redox properties of such materials are essential.

EXPERIMENTAL SECTION

Chemicals. For the synthesis of the catalysts $La(NO_3)_3{\cdot}6H_2O$ (Alpha Aesar, purity 99.9%, LOT: 61800314), $Pr(NO_3)_3{\cdot}6H_2O$ (Alpha Aesar, purity 99.9%, LOT: 61300461), $Mn(NO_3)_2{\cdot}4H_2O$ (Roth, purity ≥98%, LOT: 468274760) $Cu(NO_3)_2{\cdot}6H_2O$ (Acros Organics, purity 99%, LOT: AO374996), glycine (TCI, purity ≥99%) and deionized water, which was obtained from a laboratory purification system (Milli-Q), were employed.

Synthesis. The $A(Mn_{1-x}Cu_x)O_3$ (x = 0, 0.1, 0.2, 0.25, 0.3, 0.35, 0.4; A = La, Pr) perovskites were synthesized by solution combustion synthesis,[27,29] where glycine served both as fuel and as a complexing agent. The target batch size was 10 g. Stoichiometric amounts of metal nitrates were dissolved in distilled water together with glycine, and the ratio between the glycine and metal nitrates was fixed to 2.36 to adjust the redox potential. The clear solution was stirred for 0.5 h, quantitatively transferred into an evaporation basin, and the solvent was evaporated on a hot plate at 95 °C. The obtained foam-like resin was self-ignited on the hot plate set at 460 °C. The produced black powders (yields from 37 to 84%) were collected and calcined in a flow consisting of 20% O_2 and 80% Ar at 800 °C (flow rate 100 mL·min^{-1}, heating rate 3 °C·min^{-1}) for 6 h in a ceramic crucible positioned in a calcination tube. The sample loss during the calcination process varies between 3 and 35%. $Pr(Mn_{0.65}Cu_{0.35})O_3$, $Pr(Mn_{0.6}Cu_{0.4})O_3$, and $La(Mn_{0.6}Cu_{0.4})O_3$ were washed with diluted acetic acid (5% w/w) after the calcination to remove traces of A_2CuO_4 by-phases, followed by washing with distilled water until neutral pH. Finally, the washed samples were subjected to a second calcination process. All sample numbers allocated by an internal database of the Fritz Haber Institute, which allows a unique identification of the perovskite batches described in this work, are given in Table S1 of the Supporting Information.

Chemical Analysis. The metal content of the perovskites was determined by Inductively Coupled Plasma Optical Emission Spectroscopy (ICP OES) analysis employing an ICP OES Optima 8300 spectrometer (PerkinElmer) equipped with a Zyklon nebulizer. The samples were dissolved employing distilled water with a conductivity of 0.05 μS·cm^{-1} from ELGA pure water system (VEOLIA) and nitric acid in supra-pure quality into PTFE liners in a microwave autoclave (Anton Paar). Certified single and multielement standard solutions were employed for calibration, being each calibration based on a minimum of two points and forced through zero. The measurements have been recorded in axial mode, using water as the spectral blank and a solution of the chemical digestion without a sample as the reagent blank. Spectral evaluation is based on three points per peak. Every measurement was repeated at least three times to calculate the relative standard deviation (RSD).

The oxygen content determination was repeated three times per sample using a TCH600 setup from LECO by applying the inert gas fusion technique and employing 10 mg of each catalyst, which was heated to 3000 °C in a He stream in a graphite crucible. CO and CO_2 formed by the reaction of the oxygen in the sample with the crucible were detected by an IR cell. Y_2O_3 was used for calibration.

Scanning Electron Microscopy and Energy-Dispersive X-ray Mapping. SEM images were obtained using a Hitachi S-4800 microscope equipped with a cold field emission gun. For imaging, 1.5 kV acceleration voltage and 4 mm working distance were set to display the image by using both upper and lower secondary electron detectors. EDX mapping was also done, setting the acceleration voltage to 15 kV and the working distance to 10 mm. An energy-dispersive QUANTAX 800 EDX spectrometer working with an XFlash6|30 detector has been used to map the elemental distribution. Usually, mapping was done for 2 min when sufficient counts were gained (>10 kps). Recorded spectra were analyzed considering all found peaks, and corresponding elemental ratios were calculated for each map/spectrum. Standard deviations were calculated based on the results of all maps.

X-ray Diffraction. The phase identification of the samples was performed with powder X-ray diffraction (XRD) measurements on a Bruker AXS D8 Advance II θ/θ diffractometer (Bragg−Brentano geometry, Ni-filtered Cu Kα radiation, position-sensitive energy-dispersive LynxEye silicon strip detector). The sample powder was filled into the recess of a cup-shaped sample holder with the surface of the powder bed aligned with the edge of the sample holder (front loading). The powder XRD data were analyzed and the lattice parameters were calculated using full pattern fitting according to the Rietveld method as implemented in the TOPAS software (TOPAS version 5, copyright 1999−2014 Bruker AXS).

In order to compare the different lattice parameters of the perovskites with each other, as well as between perovskite cells of different symmetries, it is useful to normalize these parameters according to their geometric relation with the ideal cubic perovskite cell. For the orthorhombic $GdFeO_3$ type in setting *Pbnm*, we thus define:

https://doi.org/10.1021/acs.chemmater.4c00136
Chem. Mater. XXXX, XXX, XXX−XXX

$$a' = \frac{a}{\sqrt{2}} \quad (1)$$

$$b' = \frac{b}{\sqrt{2}} \quad (2)$$

$$c' = \frac{c}{2} \quad (3)$$

while for the rhombohedral $LaAlO_3$ type in a hexagonal coordinate system (R-3cH), we use:

$$a' = \frac{a}{\sqrt{2}} \quad (4)$$

$$c' = \frac{c}{\sqrt{12}} \quad (5)$$

The normalized unit cell volume is given by

$$V' = \frac{V}{Z_{ABO_3}} = a'b'c' \quad (6)$$

with Z_{ABO_3} being the number of formula units ABO_3 in the cell. Furthermore, we use the pseudocubic lattice parameter:

$$a^* = \sqrt[3]{V'} \quad (7)$$

which represents the geometric mean of the normalized lattice parameters but may also be regarded as the cell parameter a of a virtual cubic cell with the same normalized volume as the actual unit cell.

Finally, we measure the (dis-)similarity of the normalized cell parameters by defining the cell distortion parameter:

$$\Delta' = \sqrt{\frac{(a' - a^*)^2 + (b' - a^*)^2 + (c' - a^*)^2}{3}} \quad (8)$$

Thus, Δ' is defined in analogy to a standard deviation, with the minor difference that the geometric mean a^* is used as reference value instead of the arithmetic mean.

Near-Edge X-ray Absorption Fine Structure Spectroscopy. Data were collected at room temperature in vacuum at the beamlines ISISS and BElChem-PGM at the synchrotron radiation facility BESSY II of the Helmholtz–Zentrum Berlin.[30] The sample powder was pressed into thin self-supporting discs. NEXAFS was conducted at the Mn $L_{3,2}$-edges by moving the monochromator continuously with a speed of 0.23 eV per second during data recording. The exit slit of the beamline has been 111 and 180 μm for the measurements at the ISISS and BElChem-PGM beamline, respectively. The lens housing of the Ambient Pressure X-ray Photoelectron (AP-XPS) spectrometer was biased with +90 V and used as a Faraday cup to collect the NEXAFS in the total electron yield (TEY) mode for $La(Mn_{1-x}Cu_x)O_3$. For $Pr(Mn_{1-x}Cu_x)O_3$, the AP-XPS electron spectrometer was set to a fixed kinetic electron energy of 385 eV at a pass energy of 50 eV to collect the Mn L-NEXAFS in the Auger electron yield (AEY) mode. A linear background has been fitted to the pre-edge region and subtracted. The edge jump intensity has been normalized at 649 eV. The NEXAFS has been analyzed by determining the contribution of Mn^{2+}, Mn^{3+}, and Mn^{4+} species. A linear combination of reference spectra was applied to simulate the experimental spectra according to a fit procedure of Mn-based perovskites described in a previous work using the WinXAS 4.0 software package.[31,32] The average Mn oxidation state of each sample was calculated and plotted as a function of the copper content (Figure S1a). The reference spectra used and their contribution in each fit can be found in Figures S1b–f.

X-ray Photoelectron Spectroscopy. XPS spectra were recorded at room temperature using nonmonochromatized Al Kα (1486.6 eV) or Mg Kα (1253.6 eV) excitation and a hemispherical analyzer (Phoibos 150, SPECS). Instrument work functions were calibrated to give an Au $4f_{7/2}$ metallic gold binding energy (BE) of 83.95 eV, while the spectrometer dispersion was adjusted to give a BE of 932.63 eV for metallic Cu $2p_{3/2}$. Furthermore, the binding energy scale was calibrated by the standard Au $4f_{7/2}$ and Cu $2p_{3/2}$ procedure. To calculate the elemental composition, the theoretical cross sections from Yeh and Lindau,[33] the inelastic free path of the electrons from Tanuma, Powell, and Penn,[34] and the transmission function of the analyzer were used. For Cu 2p, Mn 3s, La 3d, and Pr 3d, Gaussian–Lorentzian line shapes were assumed, and a Shirley background correction was performed.[35−38] To analyze the Cu 2p and Pr 3d signals, a reference Pr 3d spectrum was acquired measuring $PrMnO_3$, while several Cu 2p spectra were recorded measuring the La-based series with the same filament as employed for Pr. Finally, the spectra for the Pr-based series were fitted by scaling the two individual fits for Pr 3d and Cu 2p with some allowance for energy position. Mn oxidation states were estimated from the Mn 3s splitting.[39] C 1s fits were based on standard C–C, C–O, and C=O binding energies.[40] The O 1s species have been fitted according to the model reported by Koch et al.,[32] modified by fixing O 1s carbonate species intensity to those of C–O and C=O species in C 1s fitted spectrum and by fixing the Gaussian/Lorentian ratio to 75. The fitting parameters are given in a previous study,[32] and the percentage of the different oxygen species are reported in Table S2 of the Supporting Information.

Surface Area Determination. N_2 adsorption was performed at −196 °C using the Autosorb-6B analyzer (Quantachrome) after outgassing the catalysts under vacuum for 2 h at 150 °C. All data treatments were performed using the Quantachrome Autosorb software package. The specific surface area was calculated according to the multipoint Brunauer–Emmett–Teller method (BET) in the range $0.05 < p/p_0 < 0.15$, assuming a N_2 cross-sectional area of 16.2 Å^2.

Temperature-Programmed Oxidation (TPO) and Temperature-Programmed Reduction (TPR). TPO/TPR cycles were performed in a fixed-bed U-shape quartz reactor using 180 mg of the catalyst (sieve fraction 100–200 μm). The sample was positioned between two quartz wool layers supported on a quartz substrate. All samples were exposed to sequential TPO-TPR cycles to examine the amount of oxygen that can be removed and incorporated up to 300 °C and the reversibility of the redox process. The applied sequence of thermal treatments in different atmospheres is presented in Figure S2. The catalysts were first subjected to in situ calcination at 800 °C in synthetic air (O_2/He = 20/80, flow rate 50 mL·min^{-1}). Then the temperature was cooled down to room temperature in synthetic air, followed by a change of the atmosphere to He (flow rate 50 mL·min^{-1}), heating to 300 °C, holding for 2 h, and finally cooling down again to room temperature in He. After this pretreatment procedure, a minimum of three cycles of TPO and TPR were performed up to 300 °C, applying a heating rate of 5 °C·min^{-1} and using a gas composition of 0.25% O_2 in He and 5% H_2 in Ar, respectively (flow rate 50 mL·min^{-1}). At 300 °C, a holding time of 2 h was applied. The H_2 and O_2 consumption was monitored with thermal conductivity and paramagnetic detectors, respectively, built into a multichannel X-stream gas analyzer by Emerson GmbH. The IR detector downstream of the O_2 sensor ABB EL1020, is aimed to detect CO_2 during oxidation. As a water trap, a tube containing a molecular sieve was installed ahead of the TCD detector. The O_2 and H_2 detectors were calibrated with certified calibration gas mixtures and controlled with a CuO standard measurement. The controlled gas flow was maintained with mass flow controllers EL-Flow by Bronkhorst. The gases used in the experiments (Ar (99.999%) and He (99.999%)) were purified with additional Oxysorb and Hydrosorb cartridges. The averaged oxygen exchange capacity $|\Delta z|$ (molar fraction of removed and refilled oxygen) has been calculated based on the molar amount of oxygen atoms transferred during the TPO and TPR cycles using eq 9.

$$\Delta z = \frac{n_O}{n_{ABO_3}} \quad (9)$$

with n_{ABO_3} being the amount of loaded perovskite in μmol, and n_O the amount of oxygen atoms transferred during one cycle in μmol. The latter is equal to the integrated area of the detected H_2 or O_2 consumption during each cycle multiplied by a factor of 2 for TPO

https://doi.org/10.1021/acs.chemmater.4c00136
Chem. Mater. XXXX, XXX, XXX−XXX

Table 1. Summary of the Sum Formulas Calculated under Different Assumptions Based on the Metal Content Determined by ICP OES Combined with the Oxygen Content Determined Independently and the Specific Surface Areas for Calcined $La(Mn_{1-x}Cu_x)O_3$

x	(A+ B) = 2[a]	A = 1[b]	(B + B′) = 1[c]	surface area ($m^2 \cdot g^{-1}$)
0	$La_{0.99}Mn_{1.01}O_{3.00}$	$La_{1.00}Mn_{1.02}O_{3.03}$	$La_{0.98}Mn_{1.00}O_{2.98}$	11.7
0.1	$La_{1.01}(Mn_{0.89}Cu_{0.10})O_{3.27}$	$La_{1.00}(Mn_{0.87}Cu_{0.10})O_{3.23}$	$La_{1.03}(Mn_{0.90}Cu_{0.10})O_{3.32}$	6.2
0.2	$La_{1.00}(Mn_{0.80}Cu_{0.20})O_{3.01}$	$La_{1.00}(Mn_{0.80}Cu_{0.20})O_{3.01}$	$La_{1.00}(Mn_{0.80}Cu_{0.20})O_{3.01}$	6.0
0.25	$La_{0.97}(Mn_{0.79}Cu_{0.24})O_{3.14}$	$La_{1.00}(Mn_{0.81}Cu_{0.25})O_{3.24}$	$La_{0.94}(Mn_{0.76}Cu_{0.24})O_{3.05}$	5.5
0.3	$La_{0.97}(Mn_{0.75}Cu_{0.28})O_{2.95}$	$La_{1.00}(Mn_{0.77}Cu_{0.29})O_{3.05}$	$La_{0.94}(Mn_{0.72}Cu_{0.28})O_{2.86}$	4.2
0.35	$La_{0.99}(Mn_{0.66}Cu_{0.36})O_{3.12}$	$La_{1.00}(Mn_{0.66}Cu_{0.36})O_{3.16}$	$La_{0.98}(Mn_{0.65}Cu_{0.35})O_{3.09}$	9.6
0.4	$La_{0.99}(Mn_{0.59}Cu_{0.41})O_{2.99}$	$La_{1.00}(Mn_{0.60}Cu_{0.42})O_{3.01}$	$La_{0.99}(Mn_{0.59}Cu_{0.41})O_{2.97}$	5.9

[a]Stoichiometry calculated under the assumption that the sum of metals is equal to 2. [b]Stoichiometry calculated under the assumption that the amount of A is 1. [c]Stoichiometry calculated under the assumption that the amount of (B + B′) is 1.

Table 2. Summary of the Sum Formulas Calculated under Different Assumptions Based on the Metal Content Determined by ICP OES Combined with the Oxygen Content Determined Independently and the Specific Surface Areas for Calcined $Pr(Mn_{1-x}Cu_x)O_3$

x	(A + B) = 2[a]	A = 1[b]	(B + B′) = 1[c]	surface area ($m^2 \cdot g^{-1}$)
0	$Pr_{1.03}Mn_{0.97}O_{2.74}$	$Pr_{1.00}Mn_{0.95}O_{2.66}$	$Pr_{1.06}Mn_{1.00}O_{2.82}$	9.4
0.1	$Pr_{1.04}(Mn_{0.86}Cu_{0.10})O_{3.15}$	$Pr_{1.00}(Mn_{0.83}Cu_{0.10})O_{3.05}$	$Pr_{1.07}(Mn_{0.89}Cu_{0.11})O_{3.27}$	5.4
0.2	$Pr_{1.03}(Mn_{0.77}Cu_{0.20})O_{3.01}$	$Pr_{1.00}(Mn_{0.75}Cu_{0.20})O_{2.93}$	$Pr_{1.06}(Mn_{0.79}Cu_{0.21})O_{3.10}$	4.2
0.25	$Pr_{1.02}(Mn_{0.73}Cu_{0.25})O_{2.77}$	$Pr_{1.00}(Mn_{0.72}Cu_{0.25})O_{2.72}$	$Pr_{1.04}(Mn_{0.74}Cu_{0.26})O_{2.82}$	9.0
0.3	$Pr_{1.03}(Mn_{0.68}Cu_{0.29})O_{2.83}$	$Pr_{1.00}(Mn_{0.66}Cu_{0.28})O_{2.73}$	$Pr_{1.07}(Mn_{0.70}Cu_{0.30})O_{2.93}$	6.1
0.35	$Pr_{1.02}(Mn_{0.64}Cu_{0.34})O_{2.70}$	$Pr_{1.00}(Mn_{0.63}Cu_{0.33})O_{2.65}$	$Pr_{1.04}(Mn_{0.65}Cu_{0.35})O_{2.76}$	3.0
0.4	$Pr_{1.00}(Mn_{0.60}Cu_{0.39})O_{2.85}$	$Pr_{1.00}(Mn_{0.60}Cu_{0.39})O_{2.84}$	$Pr_{1.01}(Mn_{0.61}Cu_{0.39})O_{2.87}$	2.4

[a]Stoichiometry calculated under the assumption that the sum of metals is equal to 2. [b]Stoichiometry calculated under the assumption that the amount of A is 1. [c]Stoichiometry calculated under the assumption that the amount of (B + B′) is 1.

cycles and by a factor of 1 for TPR cycles, according to the stoichiometry of the chemical reaction (eq 10).

$$2H_2 + O_2 \rightarrow 2H_2O \tag{10}$$

Since the oxygen transfers of oxidation and reduction have, strictly speaking, opposite signs, we use the notation $|\Delta z|$ instead of Δz for the oxygen capacity.

Propane Oxidation. The catalytic tests were carried out using a setup for partial oxidation (Integrated Lab Solutions) with 10 fixed-bed tubular reactors (2 mm inner diameter) in parallel employing 100 mg (sieved particles, 100−200 μm) of catalyst with a total flow rate varying from 5 to 30 mL·min^{-1} in the temperature range between 260 and 300 °C. The catalysts were exposed to the oxygen-rich reaction gas mixture containing C_3H_8, O_2, Ne, and N_2 in a ratio of 5:10:2:83 vol % using mass flow controllers (Bronkhorst USA, Inc.). An online gas chromatograph was used for gas analysis (Agilent 7890A). The permanent gases CO, CO_2, O_2 and N_2 were analyzed by a combination of a Plot Q (length 30 m, 0.53 mm internal diameter, 40 μm film thickness) and a Plot-MoleSieve 5A column (30 m length, 0.53 mm internal diameter, 50 μm film thickness) connected to a TCD detector. Propane and propene were analyzed by a combination of a FFAP (length 30 m, 0.53 mm internal diameter, 1 μm film thickness) and a Plot-Q column (length 30 m, 0.53 mm internal diameter, 40 μm film thickness) connected to a FID detector. Additionally, a methanizer was installed in order to detect CO and CO_2 also at the FID detector with higher precision and accuracy with respect to the concentrations revealed by the TCD detector. The conversion of propane (X_{C3H8}) and the selectivity to products i (S_i) in percentages were determined using eqs 11 and 12, respectively, based on the total amount of carbon atoms in the product and the sum of all products formed,

$$X_{C3H8} = \frac{\sum_{i=1}^{n} N_i c_i}{\sum_{i=1}^{n} N_i c_i + 3c_{C3H8out}} \times 100 \tag{11}$$

$$S_i = \frac{N_i c_i}{\sum_{i=1}^{n} N_i c_i} \times 100 \tag{12}$$

where N_i is the number of carbon atoms in the product, and c_i is the concentration of the product in the effluent gas. The rates of C_3H_8 consumption, as well as C_3H_6, and CO_2 formation have been calculated using eqs 13−15, where W is the mass of catalyst and F the flow rate.

$$X_{C3H8} = f\left(\frac{W}{F}\right) \tag{13}$$

$$r_{C3H8} = \frac{dX_{C3H8}}{d\left(\frac{W}{F}\right)} \tag{14}$$

$$r_{CO2,C3H6} = \frac{dX_{C3H8}dS_i}{d\left(\frac{W}{F}\right)} \tag{15}$$

The initial rates of C_3H_8 consumption and C_3H_6 or CO_2 formation have been calculated by extrapolating the rates to the contact time $(W/F) = 0$, which allows the comparison of all catalysts at the same temperature decoupled from the contact time.

RESULTS AND DISCUSSION

Synthesis of Perovskite Batches in the Gram Scale. In contrast to solid-state synthesis, which usually produces sintered products with a small surface area, solution combustion synthesis is fast, easily scalable to 1−10 g of product with a medium to large specific surface area, and relatively inexpensive due to the nitrate precursors and fuels used.[29,41] The preparation of the nanostructured A-$(Mn_{1-x}Cu_x)O_3$ (x = 0, 0.1, 0.2, 0.25, 0.3, 0.35, 0.4; A = La, Pr) perovskites was optimized with respect to the amount of glycine as fuel by setting the oxygen balance to zero.[41] For this purpose, the amount of glycine as added fuel was adjusted

https://doi.org/10.1021/acs.chemmater.4c00136
Chem. Mater. XXXX, XXX, XXX−XXX

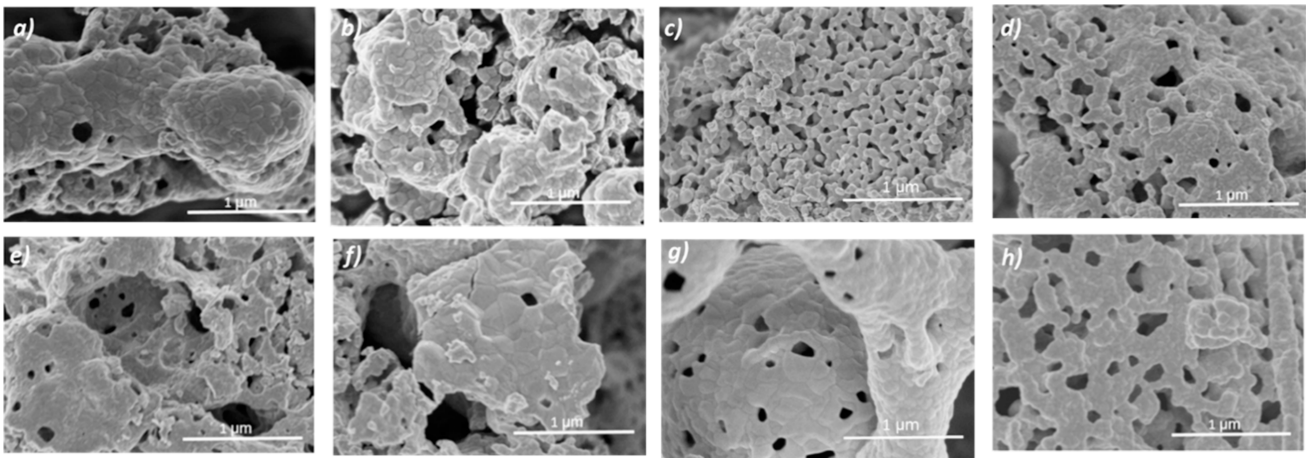

Figure 1. SEM images of calcined (a) $LaMnO_3$, (b) $La(Mn_{0.75}Cu_{0.25})O_3$, (c) $La(Mn_{0.65}Cu_{0.35})O_3$, (d) $La(Mn_{0.6}Cu_{0.4})O_3$, (e) $PrMnO_3$, (f) $Pr(Mn_{0.75}Cu_{0.25})O_3$, (g) $Pr(Mn_{0.65}Cu_{0.35})O_3$, and (h) $Pr(Mn_{0.6}Cu_{0.4})O_3$.

based on the chemical analysis of the metal nitrates used so that the available oxidizing nitrates in the metal salts formally oxidize the fuel glycine to CO_2 and N_2 during the ignition synthesis. The heating and the evaporation of the solutions, which contain metal nitrates and glycine, initiate an exothermic process that leads to spontaneous ignition and produces fine powders. The time until self-ignition of the intermediate resins at a reaction temperature of 460 °C becomes shorter with increasing Cu content, which already shows the active role of the Cu^{2+} as B′ element in changing the redox properties in comparison to unsubstituted $AMnO_3$. To avoid effects related to temperature and oxygen partial pressure, all $A(Mn_{1-x}Cu_x)O_3$ (A = La, Pr) self-ignition products were treated at the same calcination temperature of 800 °C for 6 h in flowing synthetic air. In $Pr(Mn_{0.65}Cu_{0.35})O_3$, $Pr(Mn_{0.6}Cu_{0.4})O_3$, and $La(Mn_{0.6}Cu_{0.4})O_3$, Ruddlesden−Popper by-phases A_2CuO_4 were detected in small amounts of 0.6, 6.7, and 2.1 wt %, respectively. Removal of the by-phase traces was achieved by washing with acetic acid and subsequent recalcination resulting in phase pure perovskites. For designation of the $A(Mn_{1-x}Cu_x)O_3$ (x = 0, 0.1, 0.2, 0.25, 0.3, 0.35, 0.4; A = La, Pr) perovskites in the text, table headings and figure captions, the nominal composition is always used (see Table S1 for unique sample ID's of the calcined materials).

Chemical Composition. According to chemical analysis, the targeted substitution of manganese by Cu^{2+} ions on the B-site of the synthesized perovskites was approximately achieved (Tables 1 and 2). The atom percentages of the elements determined by ICP OES analysis used for the formulas calculated under different assumptions in Tables 1 and 2 are summarized in the Supporting Information (Table S3). The broad range in nonstoichiometry of manganite perovskites[10,13,14] tolerates deviations in metal ratios in both directions, i.e., depletion at either or both metal positions to varying degrees. However, the formation of A-site vacancies is favored over the formation of B-site vacancies, as shown for $LaMnO_3$.[12] In the present work, some small deviations from the ideal values within the two series are observed. The La-based perovskites have a higher (Mn + Cu)/A ratio than the corresponding Pr-based samples (Figure S3). Contrary to some findings reported in the literature, the oxygen content does not decrease with increasing Cu substitution (Tables 1, 2, and S3), suggesting that the average oxidation state of manganese increases with increasing Cu^{2+} content.[25] Moreover, the three samples, which had been subjected to a washing process to remove traces of the A_2CuO_4 by-phase ($La(Mn_{0.6}Cu_{0.4})O_3$, $Pr(Mn_{0.6}Cu_{0.4})O_3$, and $Pr(Mn_{0.65}Cu_{0.35})O_3$), exhibit the expected ratio between A, Mn, and Cu. Thus, the washing process removes only the traces of the A_2CuO_4 by-phase and does not leach out any of the A, Mn, or Cu components.

According to SEM-EDX analysis, the elements are homogeneously distributed in the calcined materials, as exemplarily shown for low, medium, and high substitution in $LaMnO_3$, $PrMnO_3$, $La(Mn_{0.75}Cu_{0.25})O_3$, $Pr(Mn_{0.75}Cu_{0.25})O_3$, $La(Mn_{0.6}Cu_{0.4})O_3$, and $La(Mn_{0.6}Cu_{0.4})O_3$ (Figures S4−S15). Thus, as will be confirmed below using XRD data, a homogeneous distribution of the metal ions A^{3+}, Mn^{n+}, and Cu^{2+} in the bulk of the $A(Mn_{1-x}Cu_x)O_3$ perovskites can be assumed. However, STEM EDX analysis revealed the presence of some detached CuO particles for $Pr(Mn_{0.6}Cu_{0.4})O_3$, which were not detected by XRD. In Figure S16, separate peaks for the Cu and the O signals, respectively, due to exsolved CuO at the surface of $Pr(Mn_{0.6}Cu_{0.4})O_3$ are highlighted in pink within the spectrum of the line scan. In contrast, phase segregation was not observed for $La(Mn_{0.6}Cu_{0.4})O_3$ (Figure S17). The fact that segregated nanostructured CuO has been found only in the Pr-based perovskite with the highest Cu loading might indicate that the surface structure is influenced by the higher orthorhombic lattice distortion in Pr-based perovskites, which in turn is induced by the smaller size of Pr^{3+} compared to La^{3+}.

Morphology and Texture. All calcined $A(Mn_{1-x}Cu_x)O_3$ perovskites are similar in terms of their morphology. Scanning electron microscopy (SEM) imaging reveals that the materials are composed of macroporous coral-like agglomerates of nanocrystals, which form hollow tubes, hollow spheres, and irregular caves caused by the self-ignition synthesis (Figure 1). Again, no indication of any crystalline or amorphous by-phase is detected at this scale. However, with increasing Cu content in $A(Mn_{1-x}Cu_x)O_3$, the tendency to form thinner and more ramified networks (Figure 1b,c,d,f,g,h) increases compared to the unsubstituted $AMnO_3$ analogues (Figure 1a,e). The shape of the $La(Mn_{1-x}Cu_x)O_3$ particles is more regular. It encloses smaller void spaces than the examples reported in the literature, which could be attributed to the optimized synthesis conditions in the present study.[20]

The nitrogen adsorption isotherms are depicted in the Supporting Information (Figure S18). Accordingly, the

https://doi.org/10.1021/acs.chemmater.4c00136
Chem. Mater. XXXX, XXX, XXX−XXX

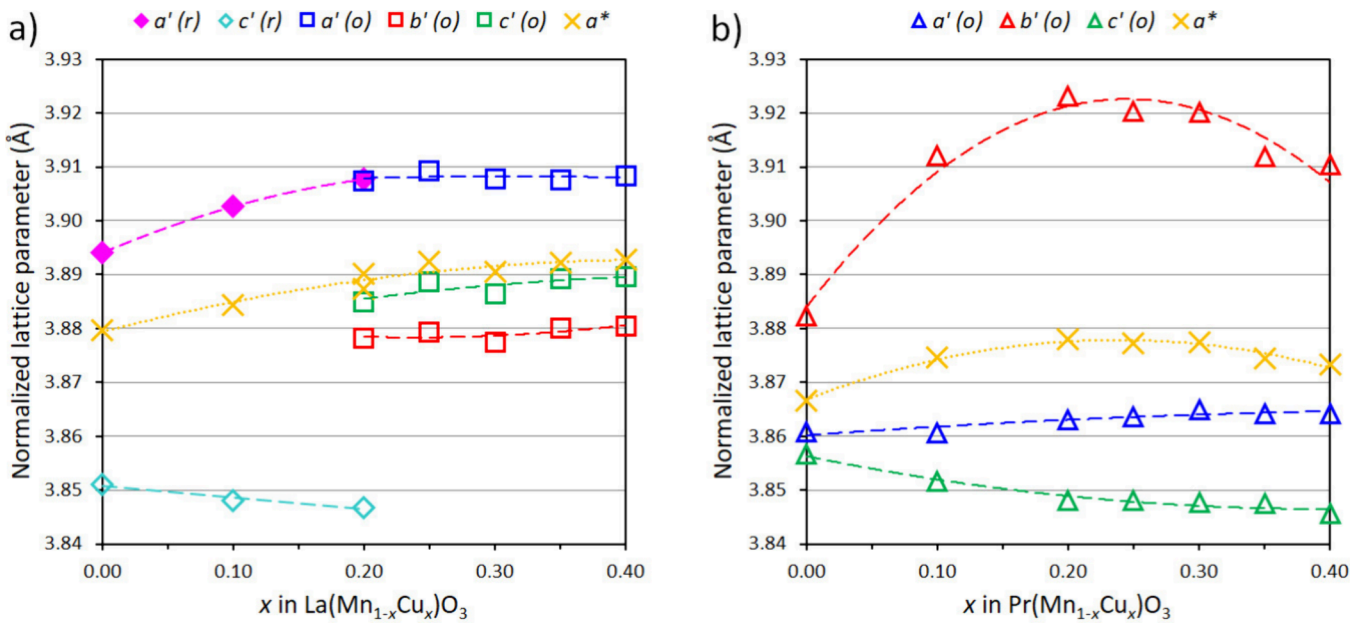

Figure 2. Normalized lattice parameters (a) of the rhombohedral (r) and O-orthorhombic (o) $La(Mn_{1-x}Cu_x)O_3$ phases and (b) of the O′-orthorhombic (o) $Pr(Mn_{1-x}Cu_x)O_3$ phases. The pseudocubic parameter a^* (yellow crosses) represents the geometric mean, providing a linear measure of normalized unit cell size. For the normalization procedure, see XRD paragraph in the Experimental Section.

perovskites exhibit macropores, which agrees well with SEM analysis. The specific surface areas of all calcined A-$(Mn_{1-x}Cu_x)O_3$ perovskites range from 2.4 to 11.7 $m^2 \cdot g^{-1}$ (Tables 1 and 2) and are in a similar order of magnitude to those of $La(Mn_{1-x}Cu_x)O_3$ compounds previously prepared by combustion synthesis methods.[18,24,25]

Crystallographic Properties of the Calcined Perovskites. The powder XRD patterns of the calcined A-$(Mn_{1-x}Cu_xO)_3$ materials show that the $La(Mn_{1-x}Cu_x)O_3$ perovskites with x = 0, 0.1, 0.2 belong to the rhombohedral $LaAlO_3$ structure type, while the rest of the La series and all members of the Pr series represent orthorhombic $GdFeO_3$ type structures. During the Rietveld refinement of the La-$(Mn_{0.8}Cu_{0.2})O_3$ data, it turned out that an additional orthorhombic minority phase had to be added to obtain a satisfactory fit. For the orthorhombic structures, the broadening of the reflections was observed to be anisotropic, especially for the members of the Pr series. The best fits of the peak profiles were obtained using a combination of isotropic size broadening and anisotropic strain broadening (Stephens model).[42] The corresponding plots of the Rietveld refinements are presented in the Supporting Information (Figures S19–S32). A complete summary of the refined crystallographic parameters is provided in the Supporting Information, Tables S4–S7.

The observed structures match the general trends seen in $A^{3+}B^{3+}O_3$ perovskites when A is a rare earth element, which predominantly crystallize in the orthorhombic $GdFeO_3$ structure type. Under ambient conditions, the rhombohedral $LaAlO_3$ type is much rarer and usually occurs when comparatively large A^{3+} (usually La) are combined with small B^{3+} (Ni, Co, Al) ions. In the case of particularly small Al^{3+}, rhombohedral symmetry is also realized with the slightly smaller A elements Pr and Nd. $LaMnO_3$, however, represents a special case, as it may crystallize, depending on the synthesis conditions, in either orthorhombic or rhombohedral symmetry, with significantly variable lattice parameters. The reason for this variability lies in the potential of manganese to adopt several oxidation states (2+/3+/4+) in perovskites, which in turn enables a rich defect chemistry of A, Mn, and O sublattices. On the one hand, $LaMnO_3$ may deviate from the ideal A:B ratio by being A-deficient, in which case vacancies in the A sublattice are balanced by Mn adopting an average oxidation state between 3+ and 4+.[43] On the other hand, even $LaMnO_3$ with a stoichiometric metal ratio can be oxidized to what is commonly termed "$LaMnO_{3+\delta}$" for convenience. Regarding crystallography, however, this oxidation is realized by the simultaneous formation of A- and B-site vacancies with retention of a complete anion lattice, i.e., $La_{1-\varepsilon}Mn_{1-\varepsilon}O_3$ ($\varepsilon = \delta/(3 + \delta)$), rather than the incorporation of interstitial oxygen.[12,44,45] Finally, the d^4 high spin configuration of Mn^{3+} usually causes a Jahn–Teller distortion of the MnO_6 octahedra. This distortion can be either cooperative or not, resulting in two distinctive subtypes within the $GdFeO_3$ structure type. In stoichiometric $LaMnO_{3.00}$, as well as $LaMnO_{3+\delta}$ with small δ, the Jahn–Teller effect is expressed cooperatively and causes significant orthorhombic distortion of the crystal lattice with $b \gg a$ (setting *Pbnm*), which is either termed O′-orthorhombic or ORT1 phase, by different authors.[43,46−48] For intermediate δ, the statistical substitution of Mn^{3+} with Mn^{4+} disturbs the cooperative distortion, resulting in more similar lattice parameters with $a > b$, called O-orthorhombic, or ORT2 phase, respectively. Larger δ finally causes the crystal structure to become rhombohedral, with all Mn–O bonds being equal by symmetry. Thus, we can assume that our rhombohedral $La(Mn_{1-x}Cu_x)O_3$ perovskites with $x \leq 0.2$ are of the more oxidized type.

It has been reported in the literature that when manganese is replaced with copper in $La(Mn_{1-x}Cu_x)O_3$, the perovskite structure is preserved up to x = 0.6.[24] However, under conventional synthesis conditions (i.e., without applying high oxygen pressure), Cu will only adopt a maximum oxidation state of +2. To maintain the charge balance with an average valence of +3 at the B-site, the introduction of Cu^{2+} changes an

https://doi.org/10.1021/acs.chemmater.4c00136
Chem. Mater. XXXX, XXX, XXX−XXX

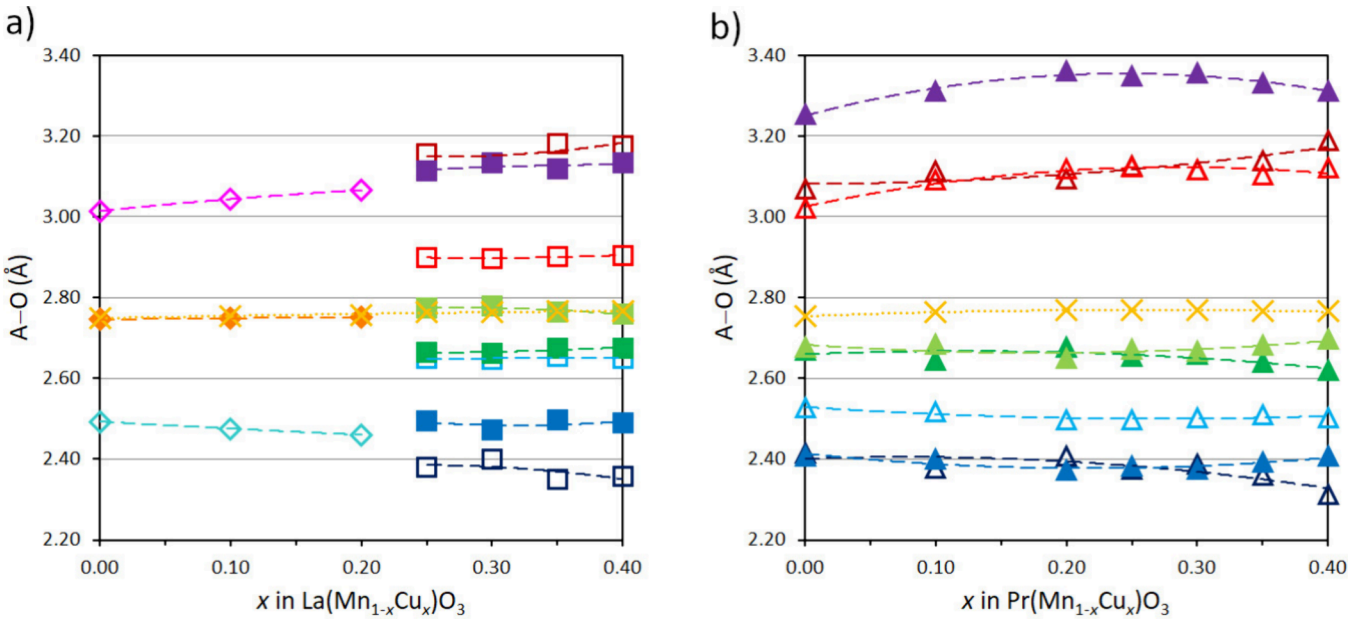

Figure 3. Individual distances A−O in $A(Mn_{1-x}Cu_x)O_3$ for (a) A = La and (b) A = Pr. Diamonds represent rhombohedral, and squares and triangles represent orthorhombic phases, respectively, while yellow crosses correspond to mean values ⟨A−O⟩. Filled symbols indicate double weight (due to higher multiplicity) compared to open symbols (rhombohedral: 6× vs 3× , orthorhombic: 2× vs 1×). The same colors are used for corresponding distances in both series. Dashed lines are intended to guide the eye.

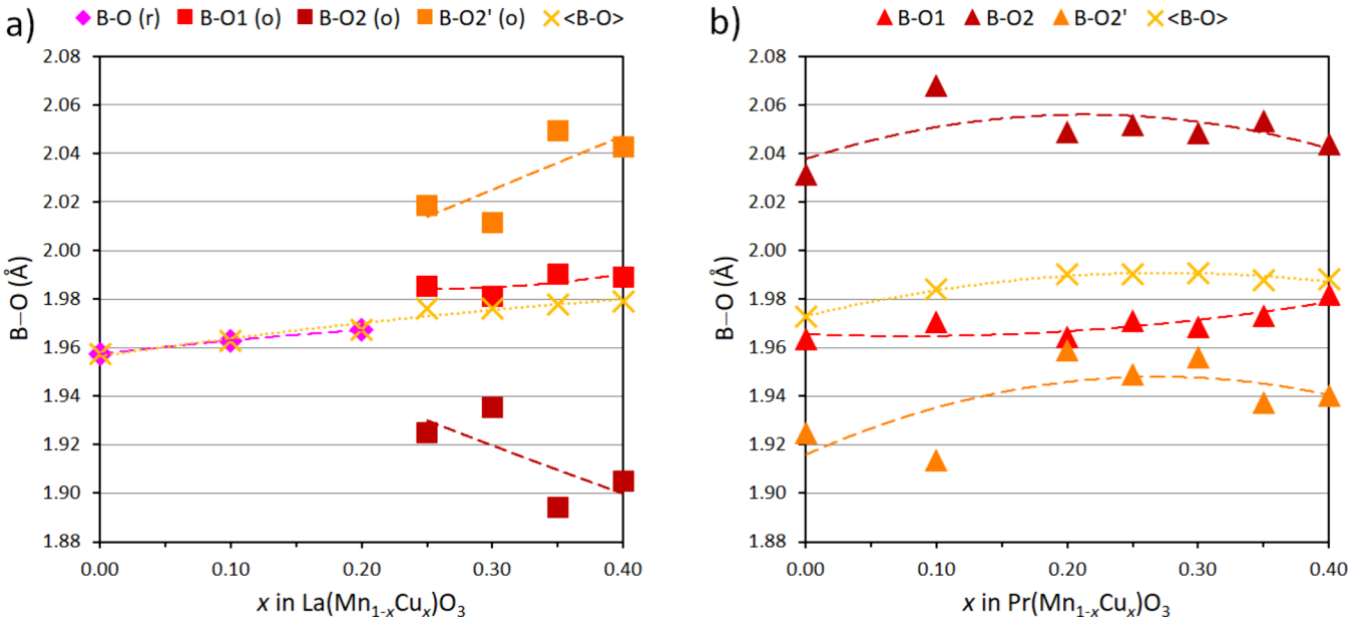

Figure 4. Individual and mean distances B−O (B = $Mn_{1-x}Cu_x$) in (a) $La(Mn_{1-x}Cu_x)O_3$ and (b) $Pr(Mn_{1-x}Cu_x)O_3$. Diamonds represent rhombohedral (r), and squares and triangles represent orthorhombic (o) phases, respectively, while yellow crosses indicate mean values. Dashed lines provide guidance to the eye.

equal amount of manganese from +3 to +4, i.e., $A(Mn^{3+}_{1-2x}Mn^{4+}_{x}Cu^{2+}_{x})O_3$. At $x = 0.5$, all available manganese is oxidized to +4, thus setting an upper limit for substitution. The presence of cation vacancies, whether caused by A deficiency or oxidation, would increase the initial average Mn oxidation state and hence lower this substitution limit even further. In our own synthesis attempts, phase pure $La(Mn_{0.5}Cu_{0.5})O_3$ proved difficult to obtain reproducibly, while single phase $Pr(Mn_{0.5}Cu_{0.5})O_3$ was not to be obtained at all. Thus, we regard the aforementioned report of $La(Mn_{0.4}Cu_{0.6})O_3$ with some skepticism,[24] attributing it to a limited sensitivity for secondary phases.

For a convenient comparison of the unit cell dimensions between different symmetries, we use normalized unit cell parameters (Figure 2) as defined in the Experimental Section. In the $La(Mn_{1-x}Cu_x)O_3$ series (Figure 2a), rhombohedral structures are observed up to $x = 0.2$, where already a significant amount of orthorhombic phase is present. At higher values of x, the lattice parameters show moderate orthorhombic distortion with $a' > c' > b'$, corresponding to the O-orthorhombic phase. In contrast, the $Pr(Mn_{1-x}Cu_x)O_3$ series

https://doi.org/10.1021/acs.chemmater.4c00136
Chem. Mater. XXXX, XXX, XXX−XXX

(Figure 2b) exhibits a significantly stronger orthorhombic distortion with $b' \gg a' > c'$ over the whole range of x, thus being of O′-orthorhombic type. Despite these differences, both series have in common that the lattice parameters changes with x are more pronounced in the region $0 < x < 0.2$, while they become quite subtle and nonmonotonous in the $0.2 < x < 0.4$ range. The pseudocubic parameter a^*, which is a convenient measure for the overall size of the (normalized) unit cell, is generally smaller for the Pr series compared to its La counterparts. This contraction of the cell volume is mainly caused by a stronger octahedral tilt, which in turn may be intuitively attributed to the smaller ionic radius of Pr^{3+}.

The mean values with corresponding standard deviations of selected interatomic distances and angles in the refined perovskite crystal structures are summarized in Table S8. Figure 3 shows the individual A−O distances and their mean values for the La and Pr series, obtained by Rietveld refinement. Despite the smaller ionic radius of Pr^{3+} compared to La^{3+}, the mean distances ⟨A−O⟩ are quite similar in both series because all 12 A−O distances of the distorted cuboctahedron are included in this average. In the Pr series, a pronounced gap between eight shorter and four longer bonds can be seen. This corresponds to a differentiation into a first and second coordination shell, resulting in an effective coordination number of eight. In contrast, the La series shows a much less distinct gap between nine shorter and three longer distances, corresponding to a coordination number of nine. If only the first coordination shells are considered, then Pr^{3+} is actually smaller than La^{3+}, in line with expectation.

The individual and mean B−O distances of both perovskite series are compared in Figure 4, revealing significant differences in the distortion of the BO_6 octahedra. In $Pr(Mn_{1-x}Cu_x)O_3$, B−O2 is much longer than the other two bonds, with B−O2′ slightly shorter than B−O1, representing a Jahn−Teller elongated octahedron. In contrast, the orthorhombic representatives of $La(Mn_{1-x}Cu_x)O_3$ exhibit an approximately inverse arrangement, with compression along the B−O2 bond axis. Surprisingly, the mean value ⟨B−O⟩ in the Pr series is larger than that of its La homologues for any given x. This seems counterintuitive because in a simple hard sphere model, the B−O distance should only depend on the nature of B, not on the type of A. This demonstrates the limits of the fixed ionic radii picture, as the B−O distances apparently respond with some degree of flexibility to the stronger strain caused by the larger octahedral tilt in the Pr series.

Since the sequences of both the B−O bond lengths (Figure 4) and the normalized lattice parameters (Figure 2) differ between the La and Pr series, we tried to trace the connection between the distortions of the BO_6 octahedra and the orthorhombic unit cells. As can be seen in Figure 5, the B−O2 and B−O2′ bonds lie roughly in the a,b-plane, approximately at 45° angles between the two axes. The tilting of the BO_6 octahedra, however, inclines B−O2 slightly more toward the b axis, while B−O2′ is leaning more toward a. Apparently, this small inclination already provides sufficient leverage for the Jahn−Teller elongation of the B−O2 bond (Figure 4b) to influence the b axis more strongly than a, thus altering the relative length of the lattice parameters. The trends in selected bond angles are shown in Figure S33. In this context, it should be noted that we had also prepared a series of $La(Mn_{1-x}Cu_x)O_3$ samples calcined at 1000 °C (not included in this manuscript), where all B−O bonds became equal within experimental error. This absence of octahedral

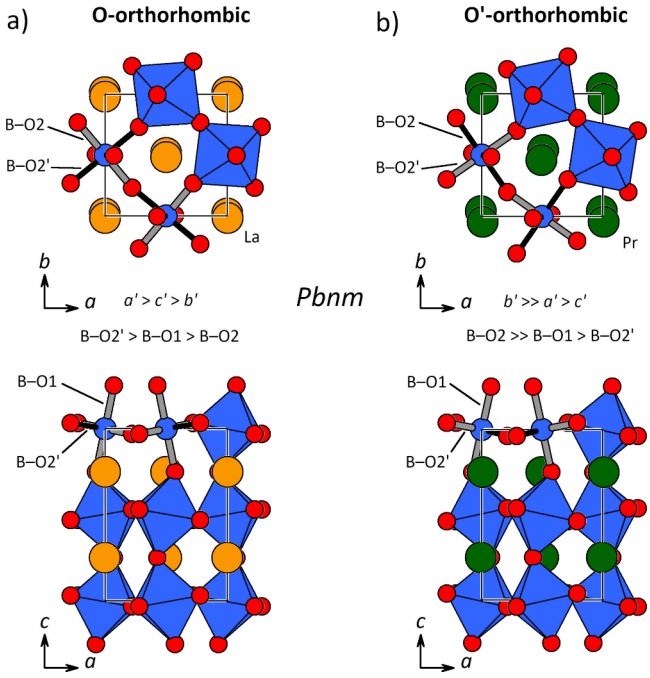

Figure 5. Comparison of the crystal structures of the corresponding orthorhombic representatives (a) $La(Mn_{0.75}Cu_{0.25})O_3$ and (b) $Pr(Mn_{0.75}Cu_{0.25})O_3$ to illustrate the differences between the O- and O′-orthorhombic variants of the $GdFeO_3$ structure type. While the difference in unit cell proportions is not readily apparent to the eye, the associated stronger octahedral tilt and larger off-center displacement of the A ions in the Pr case are clearly visible. The longest of the three distinct B−O bonds in each structure is emphasized in black. Blue balls represent the B and B′ atoms, red balls represent the O atoms, and the orange and green balls represent the A atoms La and Pr, respectively.

distortion, however, had no significant impact on the tilting or unit cell proportions compared to the 800 °C series. Hence, we may state that the octahedral compression described above for $La(Mn_{1-x}Cu_x)O_3$ is only an optional feature of the O-orthorhombic phase, while the Jahn−Teller elongation of the BO_6 octahedra in $Pr(Mn_{1-x}Cu_x)O_3$ is characteristic for the O′-orthorhombic phase.

The semirigid nature of the BO_6 octahedra, with octahedral tilting as the main degree of freedom, causes strong correlations between the structural parameters, some of which are depicted exemplarily in Figure 6. For example, we observe that for a given A element, the parameters ⟨A−O⟩ and ⟨B−O⟩ exhibit a positive, approximately linear correlation, which even includes both structure types in the La series (Figure 6a). A similar but negative correlation is found if only the A−O distances of the first coordination shell are averaged (Figure 6b). The observed tolerance factor t_{obs}, which was introduced by Sasaki et al.,[49] is based on the ratio between ⟨A−O⟩ and $\sqrt{2}$⟨B−O⟩ and measures the amount of deviation from the ideal cubic perovskite structure. In Figure 6c, it is shown that the switch between rhombohedral and orthorhombic symmetry occurs around $t_{obs} \approx 0.99$ in the system studied here. Finally, since a variation of the tolerance factor causes changes in the amount of octahedral tilting, which is accomplished by variable bending of the B−O−B angles, another correlation is observed between the mean angle ⟨B−O−B⟩ and t_{obs} (Figure 6d).

https://doi.org/10.1021/acs.chemmater.4c00136
Chem. Mater. XXXX, XXX, XXX−XXX

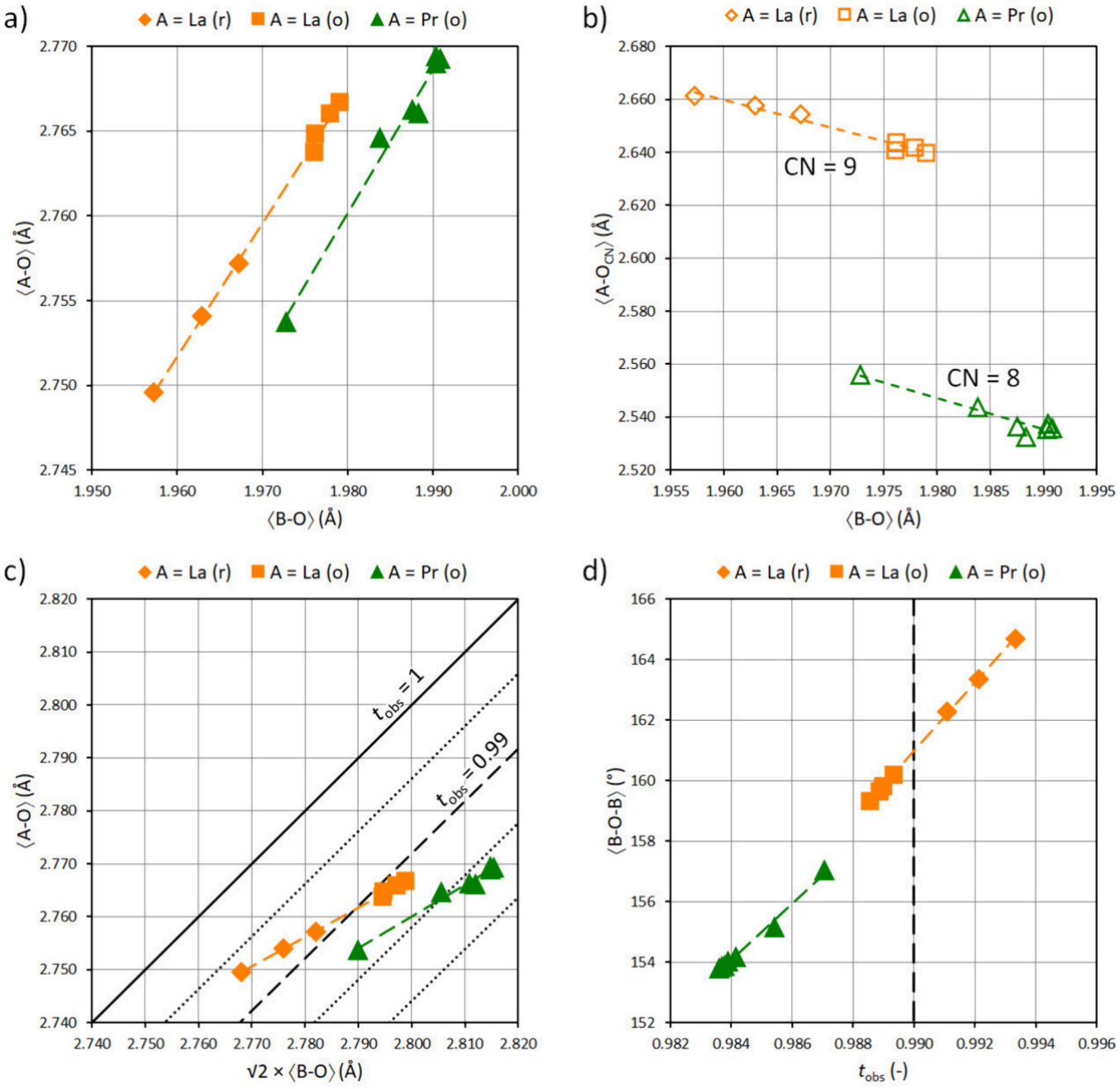

Figure 6. Parameter correlations in $A(Mn_{1-x}Cu_x)O_3$ (A = La, Pr) perovskites: (a) Approximately linear relation between mean distances ⟨A−O⟩ and ⟨B−O⟩, and (b) corresponding plot for the first coordination shell ⟨$A-O_{CN}$⟩ (La: CN = 9, Pr: CN = 8) only. (c) Alternative representation of ⟨A−O⟩ vs $\sqrt{2}$⟨B−O⟩ in the context of the observed tolerance factor t_{obs}. A solid line indicates the ideal cubic perovskite structure (t_{obs} = 1), while the broken line at t_{obs} = 0.99 separates rhombohedral from orthorhombic structures. Additional dotted lines are drawn at t_{obs} intervals of 0.005 for orientation. (d) Relation between the mean angle ⟨B−O−B⟩ and t_{obs}. Diamond symbols represent $La(Mn_{1-x}Cu_x)O_3$ with rhombohedral structure, squares represent $La(Mn_{1-x}Cu_x)O_3$ with O-orthorhombic structure, and tringles represent $Pr(Mn_{1-x}Cu_x)O_3$ with O′-orthorhombic structure.

To briefly summarize the discussion above, it can be stated that the substitution of Mn by Cu in $A(Mn_{1-x}Cu_x)O_3$ perovskites causes structural changes that are not linear, or monotonous, with the parameter x. Also, no influence of the size of the A element on the mean A−O polyhedral size can be observed. The most likely reason is that the different local geometries of the three species Mn^{3+}, Mn^{4+}, and Cu^{2+}, two of which are Jahn−Teller ions, statistically sharing the B-site, lead to a complex superposition in the average crystal structure. On the other hand, most of the structural parameters, like mean atomic distances, mean angles, t_{obs}, etc., exhibit strong, often almost linear, correlations with each other, demonstrating the complex balance of forces in the perovskite structures.

Trends in the Metal Oxidation States of the Calcined Perovskites. The substitution of manganese by the divalent copper should be accompanied by a change in the mean oxidation state of manganese, which is three in the Cu-free perovskites studied here.[7] It can be assumed that the introduction of Cu^{2+} leads to the oxidation of the stoichiometric amount of Mn^{3+} to Mn^{4+}. NEXAFS spectra of some of the perovskites were measured at the Mn L_3-edge and fitted with relevant reference compounds containing Mn^{2+},

https://doi.org/10.1021/acs.chemmater.4c00136
Chem. Mater. XXXX, XXX, XXX−XXX

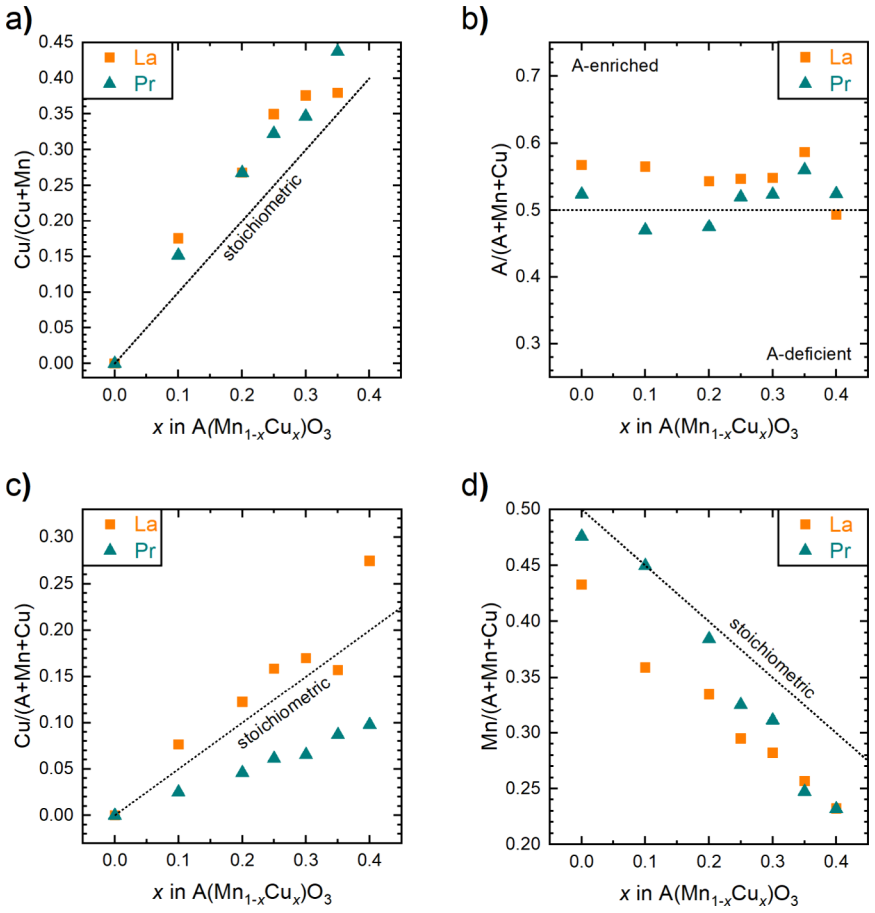

Figure 7. Atomic ratios of the elements in the near-surface region determined by XPS as a function of the nominal Cu content: (a) Cu/(Cu + Mn), (b) A/(A + Mn + Cu), (c) Cu/(A + Mn + Cu), and (d) Mn/(A + Mn + Cu).

Mn^{3+}, and Mn^{4+} species (Figure S1). Regardless of the type of A, the average oxidation state of Mn^{n+} increases linearly (black dotted line in Figure S1a) with increasing Cu content and corresponds to the expected oxidation state (gray dotted line corresponds to the theoretical values). The Mn^{4+} content, i.e. the average oxidation state of Mn^{n+}, is therefore determined by the Cu content.

The depth of information of the NEXAFS measurements is about 6 nm. In order to compare these values with the oxidation state near the surface, the perovskites were examined by photoelectron spectroscopy. The core level spectra of La, Pr, Mn, Cu, O, and C are presented in Figures S34−S38. They are in qualitative agreement with the literature.[19] Accordingly, Cu is present exclusively in the oxidation state 2+ and La and Pr in the oxidation state 3+ in the surface region.

The average surface Mn oxidation state was estimated based on the Mn 3s splitting (Table S9 and Figure S39).[39] It varies between 2.1 and 3.5 and is lower than expected based on the bulk stoichiometry of Cu, especially for the La-based series. For the Pr-based series, the average oxidation state of Mn^{n+} increases with increasing copper content except for the $Pr(Mn_{0.65}Cu_{0.35})O_3$ sample (Table S9). No trend is observed for the La-based series, perhaps due to the higher number of surface defects, which could occur as clusters of vacancies, each bound to two Mn^{2+} ions in the $3d^5$ configuration. In such a case, the formation of oxygen vacancies on the surface would be accompanied by the reduction of Mn^{3+} ions to Mn^{2+}, which would explain why the average oxidation state does not increase with the increasing Cu content.[50] Another explanation could be that the formation of holes in the O 2p states (d^4 L-ground state configuration) could lead to a decrease in Mn 3s splitting, although the formal valence of Mn increases.[39] In summary, also the surface oxidation states do not scale linearly with the parameter *x*.

Chemical Composition at the Surface. The Cu content in the surface region determined by X-ray photoelectron spectroscopy is generally higher compared to the nominal bulk values (Figure 7a, Table S10). However, in almost all perovskites, the most abundant metal atoms on the surface are the A atoms (Figures 7b and S40), especially in the La series. An exception is $La(Mn_{0.6}Cu_{0.4})O_3$, which could be due to the loss of La during the washing process in which the by-phase La_2CuO_4 was removed, even though this was not evident from the bulk analysis. Considering only the Cu content, the surface region of the La series is enriched in copper in almost all cases compared to the theoretical values, while the surface of the Pr series is depleted in Cu (Figure 7c). All surfaces have lower Mn content than would be expected based on ideal $A(B_{1-x}B'_x)O_3$ stoichiometry (Figure 7d).

The strong Jahn−Teller distortion in $Cu^{II}O_6$ octahedra could be the reason for the Cu enrichment in the surface region of the La series. The distorted $Cu^{II}O_6$ octahedron has more space when it is on the surface of the solid and not subjected to the strain of the surrounding less distorted MnO_6 octahedra and A^{3+} cations, as it is the case in the bulk. Although this should also be true for the Pr series, it is not

https://doi.org/10.1021/acs.chemmater.4c00136
Chem. Mater. XXXX, XXX, XXX−XXX

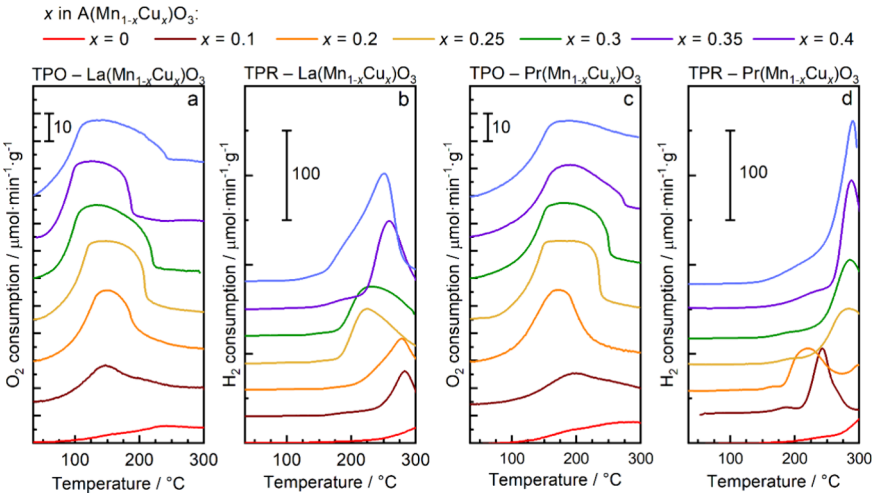

Figure 8. Profiles of the second TPO and TPR cycles for (a) TPO of $La(Mn_{1-x}Cu_x)O_3$, (b) TPR of $La(Mn_{1-x}Cu_x)O_3$, (c) TPO of $Pr(Mn_{1-x}Cu_x)O_3$, and (d) TPR of $Pr(Mn_{1-x}Cu_x)O_3$.

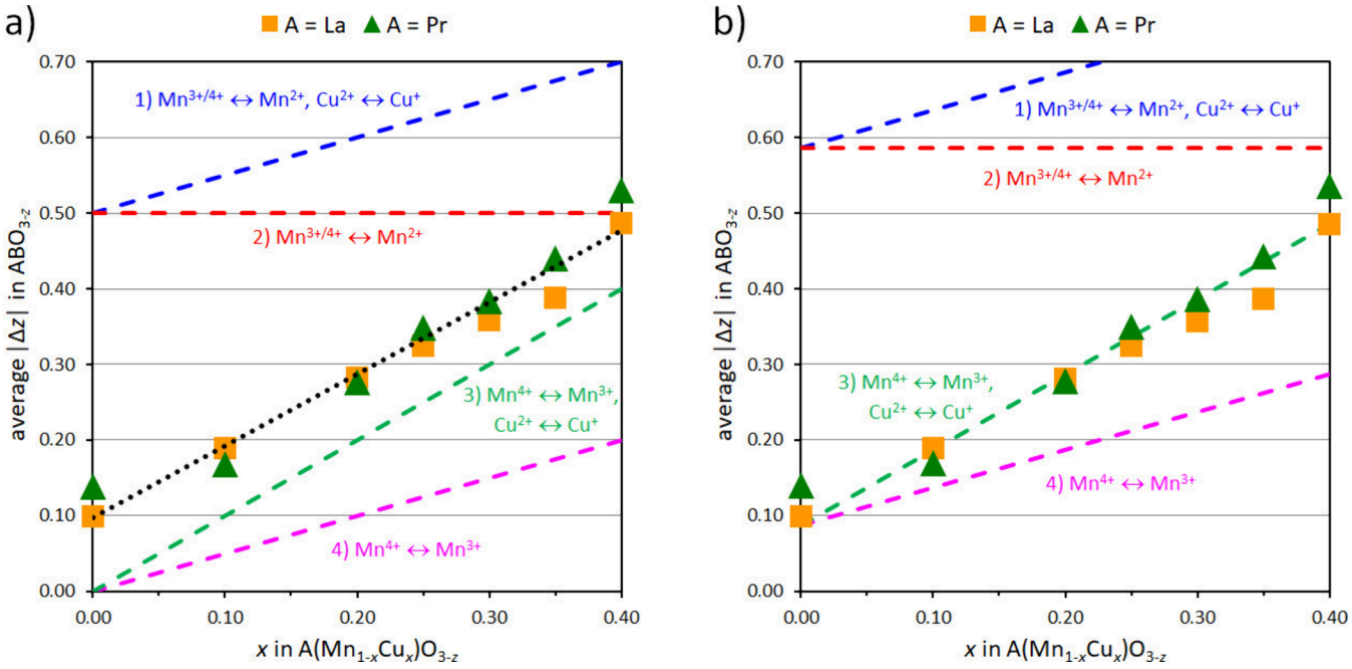

Figure 9. Molar fraction $|\Delta z|$ of reversibly exchangeable oxygen at 300 °C as a function of the copper content x: (a) initial model based on $A(Mn_{1-x}Cu_x)O_{3.00}$ (A = La, Pr) stoichiometry for the starting materials, and (b) refined model assuming $A(Mn_{1-x}Cu_x)O_{3-x}$ (A = La, Pr) as the reduced state. The colored broken lines represent different theoretical redox scenarios (see text for details) for comparison with the observed trend (black dotted line).

observed (Figure 7c). The low Cu concentration measured on the samples containing Pr (Figure 7c) could be due to errors in the cross-section taken from the literature for the lanthanides.[33] In addition, about 5−13 at% of the surface oxygen atoms belong to carbonates (Table S2), which may also introduce errors in the determination of the surface composition for all samples and reduce the depth of information. However, this does not affect the general trends, which are certainly sufficiently reliable and must be taken into account in the following discussion of the functionality of $A(Mn_{1-x}Cu_x)O_3$ perovskites in redox reactions.

Redox Properties. From the structural and surface analysis it becomes clear that there is no simple relation between the chemical composition and the defect structure of the perovskites. The redox behavior of the $A(Mn_{1-x}Cu_x)O_3$ perovskites was investigated by TPO/TPR cycles to quantify the amount of oxygen that can be removed with hydrogen and replenished reversibly with oxygen in a temperature range relevant for catalysis. After in situ calcination to remove potential adsorbates, the samples were first heated to 300 °C in helium to check whether the samples would already lose some oxygen at this temperature in an inert atmosphere. However, as no oxygen was consumed within the limits of detection during the following temperature-programmed oxidation of the first cycle, this is apparently not the case. From the first reduction on, oxygen is reversibly removed from the perovskite structure and then reintegrated during TPO in the next cycle. Hence, the second TPO/TPR cycle is shown exemplarily in Figure 8, while the full set of measured oxygen and hydrogen consumption profiles is shown in the Supporting Information,

https://doi.org/10.1021/acs.chemmater.4c00136
Chem. Mater. XXXX, XXX, XXX−XXX

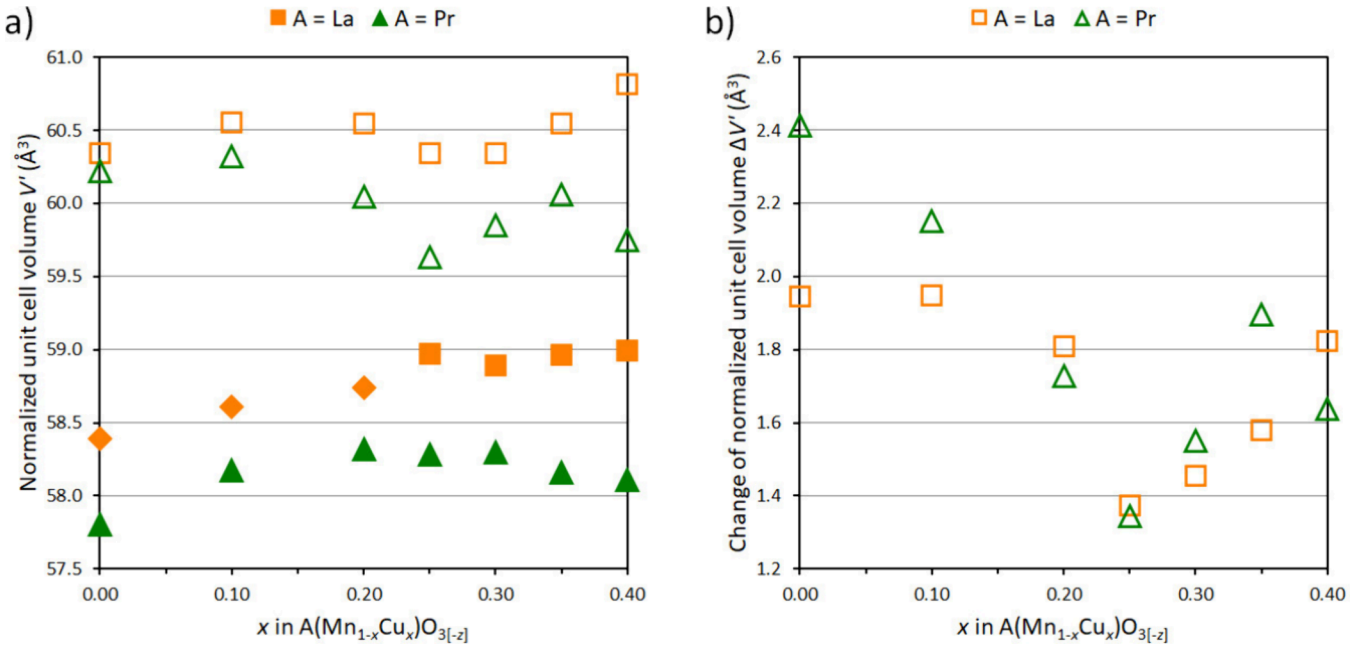

Figure 10. (a) Normalized unit cell volumes V' as a function of Cu substitution x. Full symbols represent calcined and empty symbols reduced samples. (b) Resulting volume change (difference) between oxidized and reduced states. In the case of phase mixtures (cf. Table S12), only the majority phases are considered.

Figures S41−S48. The onsets of the TPO profiles shift slightly to lower temperatures with increasing Cu content x in both series, but no corresponding systematic trend is observed for the TPR profiles.

Figure S49 shows the temporal evolution of oxygen transfer during the individual cycles. While it seems that in several cases the first TPR values are slightly larger than in the subsequent steps, we found no statistically significant support for this notion. Since no clear decreasing or increasing trend is observed, we conclude that the oxygen transfer values are stable within the limits of experimental precision, demonstrating that the redox process is essentially reversible. Hence, the results of the individual measurements were averaged to obtain more robust data (Table S11), which are displayed in Figure 9. While the absolute amount of oxygen transferred can be calculated directly from the experiment, assignment to the perovskite formula requires knowledge of the formula of the starting material or the reduced state and thus the exact composition. Since neither was known a priori with sufficient precision, we started with the simplified assumption that initially, all perovskites were of $ABO_{3.00}$ type (Figure 9a). Thus, in undoped perovskites, the oxidation state of the manganese is 3+.[7] The introduction of copper causes equimolar amounts of Mn^{3+} to change to Mn^{4+} because it follows that $B^{3+} = (Mn^{3+}{}_{1-2x}Mn^{4+}{}_{x}Cu^{2+}{}_{x})$ for charge balance reasons. This assumption is supported by the NEXAFS measurements (Figure S1a). As it was not clear which of the two B elements was reduced to which oxidation state, we calculated several theoretical redox scenarios for comparison with the experimental values. Full reduction to metallic Cu and thus exsolution of Cu particles and decomposition of the perovskite structure was not observed, neither by electron microscopy nor by XRD. If both $Mn^{3+/4+}$ would be reduced to Mn^{2+}, and Cu^{2+} to Cu^{+}, then the oxygen transfer should vary according to $|\Delta z| = 0.5x + 0.5$ (Scenario 1). If only manganese was reduced to Mn^{2+}, $|\Delta z|$ would be constant at a level of 0.5 (Scenario 2). In Scenarios 3 and 4, the reduction of manganese stops at Mn^{3+}, while Cu^{2+} is either reduced to Cu^{+} (Scenario 3) or remains Cu^{2+} (Scenario 4), leading to the relations $|\Delta z| = x$ or $|\Delta z| = 0.5\ x$, respectively. Among these four possibilities, only Scenario 3, which is shown in green in Figure 9a, approaches the observed trend. However, the experimental data show an approximately constant offset to higher values, with even the $x = 0$ samples already having an oxygen capacity of approximately 0.1. One possibility is to assume that $Mn^{3+/4+}$ would be reduced to $Mn^{2.75+}$ instead of Mn^{3+}. However, there is no plausible reason why the reduction should end in a mixed valence state. Furthermore, it has been reported that the reduction of Mn^{3+} to Mn^{2+} occurs only at temperatures significantly higher than in the present experiments.[26] Another possibility is that the starting materials actually are of "$ABO_{3+\delta}$" type, with δ in the order of approximately 0.1, and thus initially contain more Mn^{4+} than caused by the Cu^{2+} substitution alone. At least for $LaMnO_3$ and its copper-substituted variants, this assumption is also in line with the XRD results discussed above. Following these considerations, we now adjust our model assuming that the reduction ideally ends with the stoichiometry $A^{3+}(Mn^{3+}{}_{1-x}Cu^{+}{}_{x})O_{3-x}$, which thus provides the basis for calculating back to the initial $ABO_{3+\delta}$ stoichiometries (Figure 9b). Since a contribution of approximately 0.1 O atoms to the total formula mass is relatively small (<1%), the experimental data points in Figure 9b differ only very slightly from the first approximation in Figure 9a. The hypothetical scenarios, however, are now shifted to higher values. For simplicity, we assume a common δ value of 0.09, corresponding to the average δ of the experimental values, in all scenarios.

To summarize these results, the oxygen capacities $|\Delta z|$ of both perovskite series are very similar to each other, i.e., independent from A, and exhibit an approximately linear dependence on the copper content x. Since the oxygen capacity is remarkably independent of A, it is therefore not

https://doi.org/10.1021/acs.chemmater.4c00136
Chem. Mater. XXXX, XXX, XXX−XXX

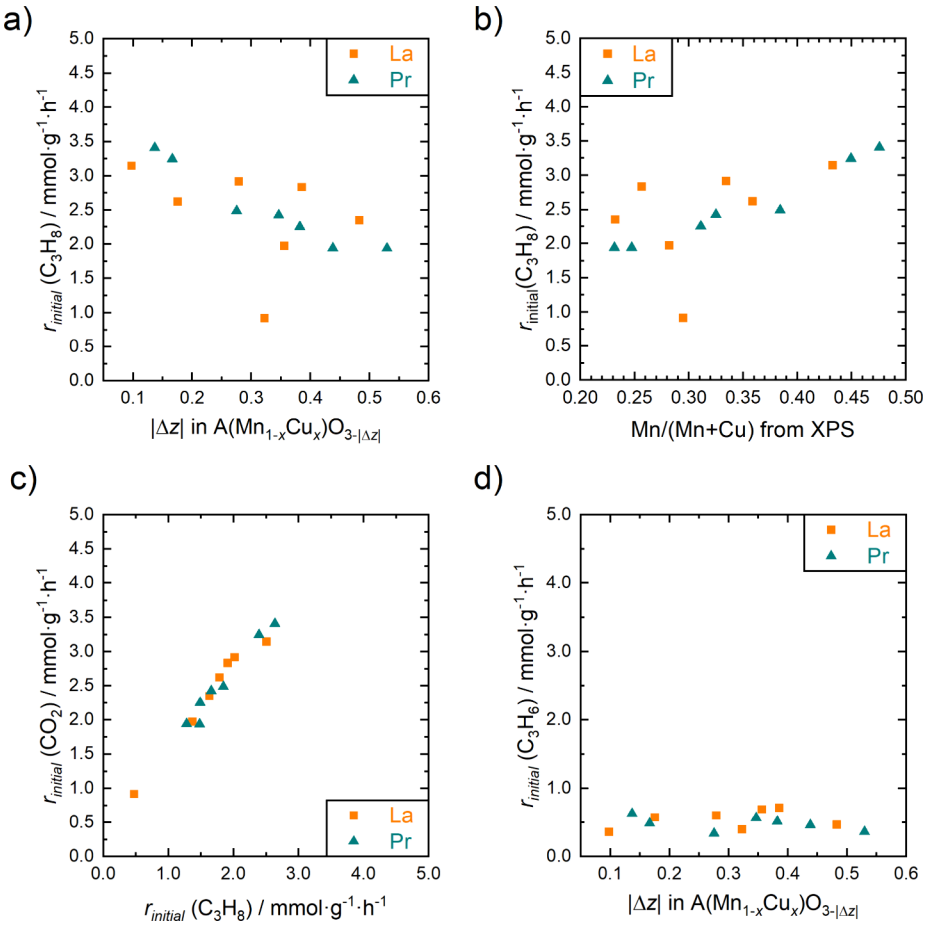

Figure 11. Propane consumption rate in propane oxidation at 300 °C (feed composition: $C_3H_8/O_2/Ne/N_2$ = 5/10/2/83) over La-based perovskites (orange squares) and Pr-based perovskites (green triangles) as a function of (a) exchangeable oxygen |Δz| determined by temperature-programmed reduction in hydrogen (Figure 8) and (b) surface fraction of Mn measured by XPS (Figure 7). Formation rate of (c) CO_2 and (d) propene as a function of the propane consumption rate and the exchangeable oxygen |Δz|, respectively. The rates are initial rates determined by extrapolation to apparent contact time of zero from contact time variation experiments at 300 °C (W/F = 0.3−1.2 g·s·mL^{-1}). The amount of exchangeable oxygen was determined based on an average of two reversible consecutive TPR-TPO cycles.

related to the different perovskite structures described above. The most plausible explanation for the observed data is that the calcined starting materials are of a moderately oxidized "$ABO_{3+\delta}$" type, with relatively similar δ values in the range 0.09 ± 0.05, which can be reversibly reduced to A($Mn_{1-x}Cu_x$)O_{3-x} containing Mn^{3+} and Cu^+. Finally, the observed oxygen capacities, being in the order of 0.1−0.5 oxygen atoms per formula unit ABO_3, exceed the capacity of (near-)surface reactions by several orders of magnitude, demonstrating the involvement of bulk lattice oxygen, as previously reported for the $La_{0.7}Sr_{0.3}MnO_3$ system.[51]

Crystallographic Changes during the Redox Process of A($Mn_{1-x}Cu_x$)O_{3-z} Perovskites. The XRD patterns of the perovskite samples after TPO/TPR cycling demonstrate that the volume structure of the perovskites investigated here changes reversibly under the conditions applied, without losing structural integrity. Overlay plots comparing the patterns of oxidized and reduced states demonstrate impressively how drastic the lattice parameters change (Figures S50−S63). Rietveld plots of the reduced samples are shown in Figures S64−S77. All reduced perovskites probably exhibit orthorhombic structures (Figures S64−S77 and Table S12). The appearance of characteristic superstructure reflections (e.g., at ca. 25° 2θ) indicates the change from rhombohedral to orthorhombic symmetry due to reduction for the corresponding La perovskites (Figures S50 and S51). Pr($Mn_{1-x}Cu_x$)O_3 with $0 \leq x \leq 0.2$ shows two overlapping perovskite phases (Figures S71−S73, Table S12). It should be noted that in several cases, the reduced perovskite phases become metrically pseudocubic. Due to the concurrent disappearance of the 111 and 021 superstructure reflections, the assignment to the $GdFeO_3$ structure type remains somewhat tentative but is more plausible in this context than a $LaAlO_3$ type structure. While all XRD patterns after TPO/TPR cycling were subjected to Rietveld refinement, the small sample amounts, admixture of quartz wool, problems with pseudosymmetry, and overlapping reflections between coexisting perovskite phases generally resulted in a lower precision of the refined atomic coordinates as compared to the initial samples. Hence, we do not discuss atomic coordinates and bond distances due to the reduced reliability, but focus on a qualitative discussion of the observed phase changes (Table S12) and the refined unit cell parameters and volumes (Table S13) instead.

Figure 10 shows that the normalized unit cell volumes increase significantly during reduction, by values between 1.3 and 2.4 Å^3 (2.2−4.0%). These volume changes, leading to the significant peak shifts seen in the XRD overlay plots (Figures S50−S63), which corroborates the TPO/TPR results con-

https://doi.org/10.1021/acs.chemmater.4c00136
Chem. Mater. XXXX, XXX, XXX−XXX

cerning the reversible removal of bulk lattice oxygen. While it seems counterintuitive at first that the removal of atoms from a crystal lattice would result in a volume increase, this observation can be explained by the increase of the B^{n+} ionic radii upon reduction of the positive charge. Furthermore, an oxygen vacancy in the lattice means that the neighboring cations, whose charge was previously compensated by an anion, now face each other and experience a repulsive force across the vacancy. No direct correlation between the volume change $\Delta V'$ and the copper content x (or the oxygen capacity $|\Delta z|$) is observed, which is likely caused by the superposition of several effects on the unit cell volume, like change in mean ionic radii, amount of octahedral tilting and local vs cooperative Jahn−Teller distortion.[52] By combining the XRD and TPO/TPR results, we find that the perovskite materials investigated here show a surprising capacity to "breathe", i.e., "exhale" and "inhale" lattice oxygen reversibly.

Catalytic Properties in Propane Oxidation. The structural investigations presented above have shown that both the change of A and the partial substitution of B by B′ have a complex influence on the structural parameters of the perovskites and their redox properties. Interestingly, the molar fraction of oxygen atoms that can be exchanged reversibly up to a temperature of 300 °C, $|\Delta z|$, appears to depend only on the amount of Cu in the perovskite and not on the type of A, although the BO_6 octahedra are differently distorted with respect to La or Pr as A-site element (Figures 9 and S49). In previous studies, perovskites have shown interesting catalytic properties in alkane activation in this low-temperature range.[32] To investigate whether the structural trends and the trends in redox behavior are also reflected in catalysis, the materials were studied in the oxidation of propane (Figures 11, S78, and S79).

The apparent activation energies determined based on the consumption rate of propane are listed in Table S14. The values between 60 and 80 $kJ \cdot mol^{-1}$ are consistent with the values found for most redox-active catalysts in propane oxidation.[53]

Interestingly, there is a negative trend between the amount of exchangeable lattice oxygen and the rates of propane consumption (Figure 11a). The reaction rate decreases with increasing availability of lattice oxygen, i.e., with increasing copper content (Figure 7c) and decreasing Mn content (Figure 7d) in the bulk and on the surface, indicating that surface manganese species are active centers for propane oxidation (Figure 11b),[54] and Cu acts as a diluent. Remarkably, a discontinuity occurs exactly at the phase change of the La-containing samples. In any case, according to the observed trends in Figure 11a,b, the perovskites appear to act as support for a manganese-containing active phase in the form of a supported monolayer, as was previously observed for manganese tungstates.[54]

The reaction mainly produces CO_2 as a product of total oxidation. However, especially at low propane conversion, considerable amounts of propene are also obtained as a valuable product of oxidative dehydrogenation of propane (Figure S79). The rate of CO_2 formation measured at 300 °C for all the different catalysts linearly correlates with the rate of propane consumption (Figure 11c) showing that the catalyst composition affects only the activity, but not the selectivity, i.e., there is no correlation between surface composition and selectivity to propene. Consequently, also the rate of propene formation is independent of the amount of exchangeable lattice oxygen (Figure 11d). The bulk oxygen available under reaction conditions therefore has no negative effect on the selectivity to propene, which is a surprising observation in light of current concepts in oxidation catalysis.[55]

The different trends obtained for the consumption rate of propane and the formation rate of propene as a function of the exchangeable oxygen $|\Delta z|$ (Figure 11a,d) indicate that CO_2 and propene are formed according to different mechanisms and bulk oxygen probably does not play a role in the entire reaction network. This could be due to the low reaction temperatures.[56,57] In any case, it becomes clear that the selectivity in alkane oxidation on perovskites cannot be tuned by simply varying the chemical composition of the catalyst. Rather, the concentration of the active surface manganese oxide species, which essentially determines the reactivity (Figure 11b), depends on the bulk composition and the bulk properties in a very complex way. In order to elucidate complex reactions on sophisticated catalysts, data-centered approaches are therefore required,[58] which we will also adopt in the future for the systems investigated here.

Summary and Conclusions. Phase pure perovskites $A(Mn_{1-x}Cu_x)O_3$ with $0 \le x \le 0.4$ were prepared by solution-combustion synthesis in small intervals of x for A = La and complemented with the corresponding series A = Pr. The $La(Mn_{1-x}Cu_x)O_3$ perovskites with low Cu content (x = 0, 0.1, 0.2) belong to the rhombohedral $LaAlO_3$ structure type, while the rest of the La series represent orthorhombic $GdFeO_3$ type structures. The $Pr(Mn_{1-x}Cu_x)O_3$ perovskites, which have not yet been described, form O′-orthorhombic, $GdFeO_3$ type structures over the entire compositional range.

Substitution of Mn by Cu in $A(Mn_{1-x}Cu_x)O_3$, (A = La, Pr), perovskites causes structural changes that are not linearly correlated with the x parameter. This is due to the complex superposition of distortions in the structure presumably partly caused by interacting Jahn−Teller effects of Mn^{3+} and Cu^{2+} ions.

Furthermore, a higher local strain is observed in the Pr compounds compared to the La compounds in the entire phase range. It is expressed by the wider spread of A−O and B−O distances in the Pr-series which in turn represents a higher degree of distortion of the A-site cuboctahedron and the B-site octahedron compared to an ideal cubic perovskite structure. Additionally, the $Pr(Mn_{1-x}Cu_x)O_3$ samples are characterized by a different distortion of the BO_6 octahedra compared to the $La(Mn_{1-x}Cu_x)O_3$ samples reflected in different longest B−O distances.

The strain induced by Jahn−Teller distortion affects also the Cu/Mn ratios in the near-surface region, which is higher than the nominal ratio. However, as far as the overall composition is concerned, an enrichment of the near-surface region with A cations was detected in almost all materials.

The substitution of manganese for copper has an impact on the redox properties. A clear correlation between the degree of Cu^{2+} substitution and the amount of reversibly exchangeable oxygen $|\Delta z|$ was observed.

The removal of oxygen during reduction has an influence on the defect structure, which is partly compensated by changes in the symmetry of the bulk structures. The structural changes depend on whether A is La^{3+} or Pr^{3+}. Thus, the rhombohedral structure of $La(Mn_{1-x}Cu_x)O_3$ for $0 \le x \le 0.2$ transforms into an orthorhombic structure, and the orthorhombic structure of $Pr(Mn_{1-x}Cu_x)O_3$ for $0 \le x \le 0.2$ partially transforms into an additional orthorhombic phase. In the temperature range up to 300 °C, the perovskite materials studied here show structural

https://doi.org/10.1021/acs.chemmater.4c00136
Chem. Mater. XXXX, XXX, XXX−XXX

stability in the sense that segregation of secondary phases largely does not occur and the ability to "breathe", i.e. reversibly "exhale" and "inhale" lattice oxygen is observed.

This structural flexibility is important for the application of the perovskites as catalysts in redox reactions, such as propane oxidation. However, no direct correlation was found between specific crystallographic or bulk parameters and catalytic properties. The negative trend of activity with respect to the amount of exchangeable oxygen, which is determined by the Cu content, deviates from the common concept in oxidation catalysis of the involvement of lattice oxygen in elementary steps of alkane oxidation, and, at least for perovskites, points to a different reaction mechanism that requires further investigation. The oxidation of propane on Mn-based perovskites is clearly a surface phenomenon, which is controlled by Mn surface sites. The nature of the surface in turn depends in a very complex way on the properties of the bulk. This complexity prevents new catalysts from being discovered by simply varying the chemical composition of the catalyst.

■ ASSOCIATED CONTENT

Supporting Information

The Supporting Information is available free of charge at https://pubs.acs.org/doi/10.1021/acs.chemmater.4c00136.

List of sample IDs, raw data of chemical analysis; description of experimental procedures; raw data of SEM-EDX maps; nitrogen adsorption−desorption isotherms; all raw data of XRD measurements; detailed results of Rietveld refinements of as prepared and reduced materials and spent catalysts; NEXAFS spectra and the linear combination of Mn L_3-edge fits including the resulting average oxidation state of Mn; XPS spectra and analyzed data of XPS and valence band spectra; raw data of TPR-TPO cycles and numerical values extracted from these measurements; raw data and apparent activation energies of the catalytic test in propane oxidation; and additional references (PDF)

■ AUTHOR INFORMATION

Corresponding Author

Annette Trunschke − *Fritz-Haber-Institut der Max-Planck-Gesellschaft, 14195 Berlin, Germany;* orcid.org/0000-0003-2869-0181; Email: trunschke@fhi-berlin.mpg.de

Authors

Gregor Koch − *Fritz-Haber-Institut der Max-Planck-Gesellschaft, 14195 Berlin, Germany*

Giulia Bellini − *Fritz-Haber-Institut der Max-Planck-Gesellschaft, 14195 Berlin, Germany;* orcid.org/0009-0008-9447-0965

Frank Girgsdies − *Fritz-Haber-Institut der Max-Planck-Gesellschaft, 14195 Berlin, Germany*

Michael Hävecker − *Max-Planck-Institut für Chemische Energiekonversion, 45470 Mülheim an der Ruhr, Germany*

Spencer J. Carey − *Fritz-Haber-Institut der Max-Planck-Gesellschaft, 14195 Berlin, Germany;* orcid.org/0000-0002-3010-8181

Olaf Timpe − *Fritz-Haber-Institut der Max-Planck-Gesellschaft, 14195 Berlin, Germany*

Thomas Götsch − *Fritz-Haber-Institut der Max-Planck-Gesellschaft, 14195 Berlin, Germany;* orcid.org/0000-0003-3673-317X

Thomas Lunkenbein − *Fritz-Haber-Institut der Max-Planck-Gesellschaft, 14195 Berlin, Germany;* orcid.org/0000-0002-8957-4216

Gudrun Auffermann − *Max-Planck-Institut für Chemische Physik fester Stoffe, 01187 Dresden, Germany*

Andrey Tarasov − *Fritz-Haber-Institut der Max-Planck-Gesellschaft, 14195 Berlin, Germany*

Robert Schlögl − *Fritz-Haber-Institut der Max-Planck-Gesellschaft, 14195 Berlin, Germany*

Complete contact information is available at: https://pubs.acs.org/10.1021/acs.chemmater.4c00136

Author Contributions

The manuscript was written through contributions of all authors. All authors have given approval to the final version of the manuscript. G.K. and G.B. contributed equally.

Funding

Open access funded by Max Planck Society.

Notes

The authors declare no competing financial interest.

■ ACKNOWLEDGMENTS

Maike Hasahagen, Jasmin Deichmann and Leonie Franke are acknowledged for N_2 physisorption measurements and the BET surface area analysis. We thank Dr. Christoph Pratsch for providing a script for data reduction in the TPR/TPO analysis, Dr. Pierre Kube for his support in carrying out the kinetic measurements, and Dr. Lucas Foppa, Fritz-Haber-Institut der Max-Planck-Gesellschaft, The NOMAD Laboratory, for helpful discussions. The Helmholtz-Zentrum Berlin is acknowledged for providing beamtime (proposal numbers 191-08014 and 192-08521) and for the continuous support of the ambient pressure XPS and NEXAFS activities of the MPG at BESSY II.

■ REFERENCES

(1) Zhu, J.; Li, H.; Zhong, L.; Xiao, P.; Xu, X.; Yang, X.; Zhao, Z.; Li, J. Perovskite Oxides: Preparation, Characterizations, and Applications in Heterogeneous Catalysis. *ACS Catal.* **2014**, *4*, 2917−2940.

(2) Hwang, J.; Rao, R. R.; Giordano, L.; Katayama, Y.; Yu, Y.; Shao-Horn, Y. Perovskites in Catalysis and Electrocatalysis. *Science* **2017**, *358*, 751−756.

(3) Peña, M. A.; Fierro, J. L. G. Chemical Structures and Performance of Perovskite Oxides. *Chem. Rev.* **2001**, *101*, 1981−2018.

(4) Ohtomo, A.; Hwang, H. Y. A High-Mobility Electron Gas at the $LaAlO_3/SrTiO_3$ Heterointerface. *Nature* **2004**, *427*, 423−426.

(5) Reyren, N.; Thiel, S.; Caviglia, A. D.; Kourkoutis, L. F.; Hammerl, G.; Richter, C.; Schneider, C. W.; Kopp, T.; Rüetschi, A.-S.; Jaccard, D.; Gabay, M.; Muller, D. A.; Triscone, J.-M.; Mannhart, J. Superconducting Interfaces Between Insulating Oxides. *Science* **2007**, *317*, 1196−1199.

(6) Sun, Y.; Xu, X.; Tong, W.; Zhang, Y. Double-Exchange Ferromagnetism and Magnetoresistance in $LaMn_{1-x}Cu_xO_3$ ($x \leqslant 0.3$). *Appl. Phys. Lett.* **2000**, *77*, 2734−2736.

(7) Cortés-Gil, R.; Ruiz-González, M. L.; Alonso, J. M.; García-Hernández, M.; Hernando, A.; González-Calbet, J. M. Magnetoresistance and Ferromagnetism in Disordered $LaCu_{0.5}Mn_{0.5}O_3$ Perovskite. *Chem. Mater.* **2013**, *25*, 2100−2108.

(8) Irvine, J. T. S.; Neagu, D.; Verbraeken, M. C.; Chatzichristodoulou, C.; Graves, C.; Mogensen, M. B. Evolution of the Electrochemical Interface in High-Temperature Fuel Cells and Electrolysers. *Nat. Energy* **2016**, *1*, 15014.

(9) Yao, Y.-F. Y. The Oxidation of Hydrocarbons and CO over Metal Oxides: IV. Perovskite-type Oxides. *J. Catal.* **1975**, *36*, 266−275.

(10) Töpfer, J.; Goodenough, J. B. $LaMnO_{3+\delta}$ Revisited. *J. Solid State Chem.* **1997**, *130*, 117−128.
(11) Miyoshi, S.; Hong, J.-O.; Yashiro, K.; Kaimai, A.; Nigara, Y.; Kawamura, K.; Kawada, T.; Mizusaki, J. Lattice Expansion upon Reduction of Perovskite-type $LaMnO_3$ with Oxygen-deficit Non-stoichiometry. *Solid State Ion.* **2003**, *161*, 209−217.
(12) Tofield, B. C.; Scott, W. R. Oxidative Nonstoichiometry in Perovskites, an Experimental Survey; The Defect Structure of an Oxidized Lanthanum Manganite by Powder Neutron Diffraction. *J. Solid State Chem.* **1974**, *10*, 183−194.
(13) van Roosmalen, J. A. M.; van Vlaanderen, P.; Cordfunke, E. H. P.; Ijdo, W. L.; Ijdo, D. J. W. Phases in the Perovskite-Type $LaMnO_{3+\delta}$ Solid Solution and the La_2O_3-Mn_2O_3 Phase Diagram. *J. Solid State Chem.* **1995**, *114*, 516−523.
(14) Golikov, Y. V.; Balakirev, V. F.; Fedorova, O. M. Homogeneity Range of Samarium Manganite in Air. *Inorg. Mater.* **2005**, *41*, 1010−1012.
(15) Tanaka, H.; Misono, M. Advances in Designing Perovskite Catalysts. *Curr. Opin. Solid State Mater. Sci.* **2001**, *5*, 381−387.
(16) Royer, S.; Duprez, D. Catalytic Oxidation of Carbon Monoxide over Transition Metal Oxides. *ChemCatChem.* **2011**, *3*, 24−65.
(17) Mizuno, N.; Fujiwara, Y.; Misono, M. Pronounced Synergetic Effect in the Catalytic Properties of $LaMn_{1-x}Cu_xO_3$. *J. Chem. Soc., Chem. Commun.* **1989**, 316−318.
(18) Yasuda, H.; Fujiwara, Y.; Mizuno, N.; Misono, M. Oxidation of Carbon Monoxide on $LaMn_{1-x}Cu_xO_3$ Perovskite-type Mixed Oxides. *J. Chem. Soc., Faraday Trans.* **1994**, *90*, 1183−1189.
(19) Abdolrahmani, M.; Parvari, M.; Habibpoor, M. Effect of Copper Substitution and Preparation Methods on the $LaMnO_{3\pm\delta}$ Structure and Catalysis of Methane Combustion and CO Oxidation. *Chin. J. Catal.* **2010**, *31*, 394−403.
(20) Tarjomannejad, A.; Niaei, A.; Farzi, A.; Salari, D.; Zonouz, P. R. Catalytic Oxidation of CO Over $LaMn_{1-x}B_xO_3$ (B = Cu, Fe) Perovskite-type Oxides. *Catal. Lett.* **2016**, *146*, 1544−1551.
(21) Tabata, K.; Hirano, Y.; Suzuki, E. XPS Studies on the Oxygen Species of $LaMn_{1-x}Cu_xO_{3+\lambda}$. *Appl. Catal. A Gen.* **1998**, *170*, 245−254.
(22) Zonouz, P. R.; Niaei, A.; Tarjomannejad, A. Kinetic Modeling of CO Oxidation over $La_{1-x}A_xMn_{0.6}Cu_{0.4}O_3$ (A = Sr and Ce) Nanoperovskite-type Mixed Oxides. *Int. J. Environ. Sci. Technol.* **2016**, *13*, 1665−1674.
(23) Chan, K. S.; Ma, J.; Jaenicke, S.; Chuah, G. K.; Lee, J. Y. Catalytic Carbon Monoxide Oxidation over Strontium, Cerium and Copper-substituted Lanthanum Manganates and Cobaltates. *Appl. Catal. A Gen.* **1994**, *107*, 201−227.
(24) Rojas, M. L.; Fierro, J. L. G.; Tejuca, L. G.; Bell, A. T. Preparation and Characterization of $LaMn_{1-x}Cu_xO_{3+\lambda}$ Perovskite Oxides. *J. Catal.* **1990**, *124*, 41−51.
(25) Brown Bourzutschky, J. A.; Homs, N.; Bell, A. T. Conversion of Synthesis Gas over $LaMn_{1-x}Cu_xO_{3+\lambda}$ Perovskites and Related Copper Catalysts. *J. Catal.* **1990**, *124*, 52−72.
(26) Royer, S.; Alamdari, H.; Duprez, D.; Kaliaguine, S. Oxygen Storage Capacity of $La_{1-x}A'_xBO_3$ perovskites (with A′=Sr, Ce; B = Co, Mn)—Relation with Catalytic Activity in the CH_4 Oxidation Reaction. *Appl. Catal., B* **2005**, *58*, 273−288.
(27) Thoda, O.; Xanthopoulou, G.; Vekinis, G.; Chroneos, A. Review of Recent Studies on Solution Combustion Synthesis of Nanostructured Catalysts. *Adv. Eng. Mater.* **2018**, *20*, No. 1800047.
(28) Norby, P.; Andersen, I. G. K.; Andersen, E. K.; Andersen, N. H. The Crystal Structure of Lanthanum Manganate(III), $LaMnO_3$, at Room Temperature and at 1273 K under N_2. *J. Solid State Chem.* **1995**, *119*, 191−196.
(29) Pechini, M. P. Method of Preparing Lead and Alkaline Earth Titanates and Niobates and Coating Method using the Same to Form a Capacitor, US304434A, 1967.
(30) Sawhney, K. J. S.; Senf, F.; Scheer, M.; Schäfers, F.; Bahrdt, J.; Gaupp, A.; Gudat, W. A Novel Undulator-based PGM Beamline for Circularly Polarised Synchrotron Radiation at BESSY II. *Nucl. Instrum. Methods Phys. Res.* **1997**, *390*, 395−402.
(31) Ressler, T. WinXAS: a program for X-ray Absorption Spectroscopy Data Analysis under MS-Windows. *J. Synchrotron Rad.* **1998**, *5*, 118−122.
(32) Koch, G.; Hävecker, M.; Teschner, D.; Carey, S. J.; Wang, Y.; Kube, P.; Hetaba, W.; Lunkenbein, T.; Auffermann, G.; Timpe, O.; Rosowski, F.; Schlögl, R.; Trunschke, A. Surface Conditions That Constrain Alkane Oxidation on Perovskites. *ACS Catal.* **2020**, *10*, 7007−7020.
(33) Yeh, J. J.; Lindau, I. Atomic Subshell Photoionization Cross Sections and Asymmetry Parameters: $1 \leqslant Z \leqslant 103$. *At. Data Nucl. Data Tables* **1985**, *32*, 1−155.
(34) Tanuma, S.; Powell, C. J.; Penn, D. R. Calculations of Electron Inelastic Mean Free Paths (IMFPS). IV. Evaluation of Calculated IMFPs and of the Predictive IMFP Formula TPP-2 for Electron Energies between 50 and 2000 eV. *Surf. Interface Anal.* **1993**, *20*, 77−89.
(35) Biesinger, M. C.; Payne, B. P.; Grosvenor, A. P.; Lau, L. W. M.; Gerson, A. R.; Smart, R. S. C. Resolving Surface Chemical States in XPS Analysis of First Row Transition Metals, Oxides and Hydroxides: Cr, Mn, Fe. *Co and Ni. Appl. Surf. Sci.* **2011**, *257*, 2717−2730.
(36) Sunding, M. F.; Hadidi, K.; Diplas, S.; Løvvik, O. M.; Norby, T. E.; Gunnæs, A. E. XPS Characterisation of In Situ Treated Lanthanum Oxide and Hydroxide using Tailored Charge Referencing and Peak Fitting Procedures. *J. Electron Spectrosc. Relat. Phenom.* **2011**, *184*, 399−409.
(37) Biesinger, M. C. Advanced Analysis of Copper X-ray Photoelectron Spectra. *Surf. Interface Anal.* **2017**, *49*, 1325−1334.
(38) Ogasawara, H.; Kotani, A.; Potze, R.; Sawatzky, G. A.; Thole, B. T. Praseodymium 3d-and 4d-Core Photoemission Spectra of Pr_2O_3. *Phys. Rev. B* **1991**, *44*, 5465.
(39) Galakhov, V. R.; Demeter, M.; Bartkowski, S.; Neumann, M.; Ovechkina, N. A.; Kurmaev, E. Z.; Lobachevskaya, N. I.; Mukovskii, Y. M.; Mitchell, J.; Ederer, D. L. Mn 3s Exchange Splitting in Mixed-Valence Manganites. *Phys. Rev. B* **2002**, *65*, No. 113102.
(40) Salmeron, M.; Schlögl, R. Ambient Pressure Photoelectron Spectroscopy: A New Tool for Surface Science and Nanotechnology. *Surf. Sci. Rep.* **2008**, *63*, 169−199.
(41) Hwang, C.-C.; Tsai, J.-S.; Huang, T.-H.; Peng, C.-H.; Chen, S.-Y. Combustion Synthesis of Ni−Zn Ferrite Powder—Influence of Oxygen balance Value. *J. Solid State Chem.* **2005**, *178*, 382−389.
(42) Stephens, P. W. Phenomenological Model of Anisotropic Peak Broadening in Powder Diffraction. *J. Appl. Crystallogr.* **1999**, *32*, 281−289.
(43) Sakai, N.; Fjellvåg, H.; Lebech, B. Effect of Non-stoichiometry on Properties of $La_{1-t}MnO_{3\pm\delta}$. Part II. Crystal Structure. *Acta Chem. Scand.* **1997**, *51*, 904−909.
(44) Van Roosmalen, J. A. M.; Cordfunke, E. H. P.; Helmholdt, R. B.; Zandbergen, H. W. The Defect Chemistry of $LaMnO_{3\pm\delta}$: 2. Structural Aspects of $LaMnO_{3+\delta}$. *J. Solid State Chem.* **1994**, *110*, 100−105.
(45) Alonso, J. A.; Martínez-Lope, M. J.; Casais, M. T.; Macmanus-Driscoll, J. L.; de Silva, P. S.; Cohen, L. F.; Fernández-Díaz, M. T. Non-stoichiometry, Structural Defects and Properties of $LaMnO_{3+\delta}$ with High δ Values ($0.11 \leq \delta \leq 0.29$). *J. Mater. Chem.* **1997**, *7*, 2139−2144.
(46) Goodenough, J. B.; Wold, A.; Arnott, R. J.; Menyuk, N. Relationship Between Crystal Symmetry and Magnetic Properties of Ionic Compounds Containing Mn^{3+}. *Physi. Rev.* **1961**, *124*, 373−384.
(47) Goodenough, J. B.; Longo, M. *3.0.1 General remarks: Datasheet from Landolt-Börnstein - Group III Condensed Matter*; Hellwege, K. H.; Hellwege, A. M., Eds.; Springer-Verlag: Berlin Heidelberg, 1970, Vol. *4A*.
(48) Sakai, N.; Fjellvåg, H.; Lebech, B. Effect of Non-stoichiometry on Properties of $La_{1-t}MnO_{3\pm\delta}$. Part I. Phase Relations. *Acta Chem. Scand.* **1996**, *50*, 580−586.
(49) Sasaki, S.; Prewitt, C. T.; Liebermann, R. C. The Crystal Structure of $CaGeO_3$ Perovskite and the Crystal Chemistry of the $GdFeO_3$-type Perovskites. *Am. Mineral.* **1983**, *68*, 1189−1198.

https://doi.org/10.1021/acs.chemmater.4c00136
Chem. Mater. XXXX, XXX, XXX−XXX

(50) Van Roosmalen, J. A. M.; Cordfunke, E. H. P. A New Defect Model to Describe the Oxygen Deficiency in Perovskite-type Oxides. *J. Solid State Chem.* **1991**, *93*, 212−219.
(51) Cao, L.; Petracic, O.; Zakalek, P.; Weber, A.; Rucker, U.; Schubert, J.; Koutsioubas, A.; Mattauch, S.; Bruckel, T. Reversible Control of Physical Properties via an Oxygen-Vacancy-Driven Topotactic Transition in Epitaxial $La_{0.7}Sr_{0.3}MnO_{3-\Delta}$ Thin Films. *Adv. Mater.* **2019**, *31*, No. 1806183.
(52) Pollert, E.; Krupička, S.; Kuzmičová, E. Structural Study of $Pr_{1-x}Ca_xMnO_3$ and $Y_{1-x}Ca_xMnO_3$ Perovskites. *J. Phys. Chem. Solids* **1982**, *43*, 1137−1145.
(53) Carrero, C. A.; Schloegl, R.; Wachs, I. E.; Schomaecker, R. Critical Literature Review of the Kinetics for the Oxidative Dehydrogenation of Propane over Well-Defined Supported Vanadium Oxide Catalysts. *ACS Catal.* **2014**, *4*, 3357−3380.
(54) Li, X.; Teschner, D.; Streibel, V.; Lunkenbein, T.; Masliuk, L.; Fu, T.; Wang, Y.; Jones, T.; Seitz, F.; Girgsdies, F.; Rosowski, F.; Schlögl, R.; Trunschke, A. How to Control Selectivity in Alkane Oxidation? *Chem. Sci.* **2019**, *10*, 2429−2443.
(55) Grant, J. T.; Venegas, J. M.; McDermott, W. P.; Hermans, I. Aerobic Oxidations of Light Alkanes over Solid Metal Oxide Catalysts. *Chem. Rev.* **2018**, *118*, 2769−2815.
(56) Wang, Y.; Rosowski, F.; Schlögl, R.; Trunschke, A. Oxygen Exchange on Vanadium Pentoxide. *J. Phys. Chem. C* **2022**, *126*, 3443−3456.
(57) Haber, J. Selectivity in Heterogeneous Catalytic Oxidation of Hydrocarbons. In *Heterogeneous Hydrocarbon Oxidation*; American Chemical Society: 1996; Vol. *638*, pp. 20−34.
(58) Foppa, L.; Rüther, F.; Geske, M.; Koch, G.; Girgsdies, F.; Kube, P.; Carey, S. J.; Hävecker, M.; Timpe, O.; Tarasov, A. V.; Scheffler, M.; Rosowski, F.; Schlögl, R.; Trunschke, A. Data-Centric Heterogeneous Catalysis: Identifying Rules and Materials Genes of Alkane Selective Oxidation. *J. Am. Chem. Soc.* **2023**, *145*, 3427−3442.

https://doi.org/10.1021/acs.chemmater.4c00136
Chem. Mater. XXXX, XXX, XXX−XXX